AGU ADVANCING EARTH AND SPACE SCIENCE

JGR Oceans

RESEARCH ARTICLE
10.1029/2021JC018375

Surface Gravity Wave Interferometry and Ocean Current Monitoring With Ocean-Bottom DAS

Ethan F. Williams[1], **Zhongwen Zhan**[1], **Hugo F. Martins**[2], **María R. Fernández-Ruiz**[3], **Sonia Martín-López**[3], **Miguel González-Herráez**[3], and **Jörn Callies**[4]

[1]Seismological Laboratory, California Institute of Technology, Pasadena, CA, USA, [2]Instituto de Óptica, CSIC, Madrid, Spain, [3]Department of Electronics, Polytechnic School, University of Alcalá, Alcalá de Henares, Spain, [4]Environmental Science and Engineering, California Institute of Technology, Pasadena, CA, USA

Key Points:

- Seafloor horizontal strain measured with distributed acoustic sensing is sensitive to ocean surface gravity wave (OSGW) pressure
- Ambient noise interferometry can be used to measure the dispersion relation of OSGW and infer flow velocity
- We resolve the spatio-temporal pattern of the tidal current along a 3-km submarine cable segment in the Strait of Gibraltar

Correspondence to:
E. F. Williams,
efwillia@caltech.edu

Citation:
Williams, E. F., Zhan, Z., Martins, H. F., Fernández-Ruiz, M. R., Martín-López, S., González-Herráez, M., & Callies, J. (2022). Surface gravity wave interferometry and ocean current monitoring with ocean-bottom DAS. *Journal of Geophysical Research: Oceans*, *127*, e2021JC018375. https://doi.org/10.1029/2021JC018375

Received 21 DEC 2021
Accepted 27 APR 2022

Abstract The cross-correlation of a diffuse or random wavefield at two points has been demonstrated to recover an empirical estimate of the Green's function under a wide variety of source conditions. Over the past two decades, the practical development of this principle, termed ambient noise interferometry, has revolutionized the fields of seismology and acoustics. Yet, because of the spatial sparsity of conventional water column and seafloor instrumentation, such array-based processing approaches have not been widely utilized in oceanography. Ocean-bottom distributed acoustic sensing (OBDAS) repurposes pre-existing optical fibers laid in seafloor cables as dense arrays of broadband strain sensors, which observe both seismic waves and ocean waves. The thousands of sensors in an OBDAS array make ambient noise interferometry of ocean waves straightforward for the first time. Here, we demonstrate the application of ambient noise interferometry to surface gravity waves observed on an OBDAS array near the Strait of Gibraltar. We focus particularly on a 3-km segment of the array on the continental shelf, containing 300 channels at 10-m spacing. By cross-correlating the raw strain records, we compute empirical ocean surface gravity wave Green's functions for each pair of stations. We first apply beamforming to measure the time-averaged dispersion relation along the cable. Then, we exploit the non-reciprocity of waves propagating in a flow to recover the depth-averaged current velocity as a function of time using a waveform stretching method. The result is a spatially continuous matrix of current velocity measurements with resolution <100 m and <1 hr.

Plain Language Summary Ocean currents are challenging to measure because they are complex: flow varies across more than six orders of magnitude in space and time. The wavespeed of ocean surface gravity waves propagating in a current encodes information about the velocity of the current, providing an opportunity to measure current velocity from ocean wave records. In particular, waves propagating along the current move faster than waves propagating against the current, which is termed non-reciprocity. By cross-correlating ocean wave records at two locations, we can measure the non-reciprocity and thereby recover an estimate of the average current velocity. In this study, we employ distributed acoustic sensing to measure ocean surface gravity wave propagation along an ocean-bottom fiber optic cable. As waves pass over the cable, they exert a small force at the seafloor which deforms the cable and stretches the fiber within. By repeatedly probing the fiber with a laser, we can measure these minute deformations at each point along the fiber. We demonstrate this method on a power transmission cable in the Strait of Gibraltar, monitoring the spatio-temporal evolution of the tidal current over a period of 4.5 days.

1. Introduction

Flow occurs across a broad spectrum of space and time scales in the global oceans, from oceanic gyres ($>10^6$ m and $>10^6$ s) to small-scale turbulent mixing ($<10^{-2}$ m and $<10^1$ s). Instrumental observation of complex oceanic flows is therefore challenging. Contemporary methods are generally divided into two categories: Lagrangian and Eulerian. Lagrangian methods, including floats and drifters, are inherently multi-scale because they follow the motion of a fluid parcel. However, the spatial distribution of drifters is biased by the flow and measurements are not temporally repeatable. Eulerian methods, including moored current meters, acoustic Doppler current profilers (ADCP), and high-frequency (HF) radar, measure flow velocity relative to a fixed point. Bottom-installed ADCP and moored instruments can resolve time-dependent flow at a single location; however, deploying extensive instrument networks is often prohibitively expensive. Conversely, while radar-based methods can capture the spatial complexity of flow, they only measure the flow at the surface.

One innovative approach to ocean current measurement came in the form of ocean acoustic tomography. By comparing the acoustic travel time measured from reciprocal experiments along the same ray path, Worchester (1977) demonstrated that the path-averaged flow speed can be recovered. Repeating the experiment at regular intervals and utilizing an array of sources and receivers, along-path time delays can then be tomographically inverted for spatio-temporal variations in current speed. Ocean acoustic tomography has been employed in diverse environments across spatial scales of 10^2–10^6 m and temporal scales of 10^2–10^7 s (Dushaw et al., 1994; Howe et al., 1987; Lin et al., 2005). But, in spite of these successes, ocean acoustic tomography has not been deployed on a large scale owing to concern about the impact of repeating, active acoustic sources on marine mammals.

More recently, Lobkis and Weaver (2001) demonstrated that cross-correlations of passive recordings of a diffusive wavefield converge to the acoustic Green's function after sufficient temporal stacking, providing a non-invasive alternative to active sources. This method, termed ambient noise interferometry, was quickly adapted from the laboratory scale to global seismology in order to probe the solid Earth without the need to wait for earthquakes (Campillo & Paul, 2003; Shapiro et al., 2005). Ambient noise interferometry was subsequently applied to ocean acoustics (Brown et al., 2014; Godin et al., 2010; Roux et al., 2004). And, in an experiment in the Straits of Florida, Godin, Brown, et al. (2014) demonstrated that flow velocities could be recovered from passive hydrophone recordings using travel-time differences in reciprocal measurements. However, passive ocean acoustic tomography has not proven widely successful due to several unique challenges: the strongly time-dependent nature of the ocean environment can inhibit convergence through stacking; autonomous hydrophones can experience significant clock drift; and the relative location of hydrophones can be perturbed by local flow conditions (Brown et al., 2014; Godin, 2018).

The theory of ambient noise interferometry has also been extended to ocean surface gravity wave (OSGW; Brown & Lu, 2016; Godin, Zabotin, et al., 2014). High-frequency OSGW in the 0.03–1 Hz band, termed wind waves, are generated by wind stresses at the sea surface throughout the oceans. Wind waves from distant storms can be observed at intermediate frequencies (<0.1 Hz) as swell. Interaction of wind waves and swell with coastal bathymetry and resonance of wave groups generate lower frequency OSGW termed infragravity waves in the 0.001–0.03 Hz band, which can propagate across ocean basins (Herbers et al., 1995). Pressure perturbations from surface gravity and infragravity waves can be observed by seafloor pressure gauges, such as those often deployed with ocean-bottom seismometers (OBS), with the bandwidth determined by water depth (Webb, 1998). Harmon et al. (2012) first cross-correlated pressure gauge data from five OBS deployed offshore Sumatra and back-projected the envelope of the noise correlation functions (NCF) to determine infragravity wave source regions. Similar studies have been done by Neale et al. (2015) and Tonegawa et al. (2018) on OBS arrays offshore Cascadia and Japan. Godin, Zabotin, et al. (2014) cross-correlated a year of pressure gauge data from an array of 28 OBS deployed offshore the South Island of New Zealand and used a coherence-based transformation to measure the frequency-dependent directional spectrum of infragravity waves. Focusing instead on higher frequency waves in shallow water, Brown and Lu (2016) proved that cross-correlations of wave height time-series converged to the OSGW Green's function in a controlled wave-tank experiment, but were unable to extract coherent NCF from surface buoy data collected offshore New Jersey. No study has yet attempted to utilize OSGW interferometry to measure ocean currents, but the theory has been demonstrated by Godin (2006) whose general framework for interferometry of acoustic-gravity waves in a moving medium includes the specific case of OSGW propagating in a current.

Here, we build upon this work and propose a novel method for high-resolution measurement of ocean currents by cross-correlation of OSGWs recorded on an ocean-bottom fiber optic cable using distributed acoustic sensing (DAS). Despite the promise of passive current monitoring by acoustic or OSGW interferometry, deployment costs and logistics for autonomous hydrophones, OBS, and pressure gauges are too high for the large-N arrays that would be needed to capture multi-scale variations in flow across oceanic environments. DAS offers a competitive alternative to conventional instrumentation through re-purposing pre-existing submarine telecommunications fibers as networks of ocean-bottom sensors. A DAS system works by transmitting short laser pulses through an optical fiber and recording the backscattered light from micro-scale imperfections in the fiber. When the optical path length between scatterers is modified by deformation (such as from seismic waves, pressure transients, or acoustic vibrations), the recorded backscatter trace exhibits a coherent phase shift from one pulse to the next. The phase shifts measured from each pulse (or pair of pulses) are integrated over consecutive fiber segments and converted to units of physical strain based on a linear scaling. A DAS system thereby transforms an ordinary optical fiber into a dense array of broadband strainmeters with thousands of channels, 1–10 m channel spacing, 0.1–10 kHz sampling rates, and up to ∼100 km sensing range. Such spatial density is impossible with conventional ocean-bottom or water-column instrumentation.

Over the past decade, DAS has fueled a revolution in large-N geophysical sensing, with broad applications, from vertical seismic profiling and borehole flow monitoring with vertical arrays to receiver functions and surface wave tomography with horizontal arrays (Lindsey & Martin, 2021; Zhan, 2020). Recently, concurrent studies by Lindsey et al. (2019), Sladen et al. (2019), and Williams et al. (2019) demonstrated that DAS applied to optical fibers in submarine cables (ocean-bottom DAS or OBDAS) could record both seismological and oceanographic phenomena, observing earthquakes from local to teleseismic distances as well as local OSGW, swell, and infragravity waves. In particular, Williams et al. (2019) showed that OSGW directional spectra observed with OBDAS exhibited a clear Doppler shift indicating the presence of a current. Lindsey et al. (2019) also speculated about possible signatures of internal gravity waves and tidal bores, and later Ide et al. (2021) reported tidal signals in deep water. Yet, the oceanographic applications of OBDAS remain largely unexplored.

In this paper, we utilize the non-reciprocity of OSGW ambient noise cross-correlation functions (NCFs) computed from passive OBDAS data to measure spatio-temporal variations in ocean current velocity. In Section 2, we introduce our data set, a 4.5-day DAS recording from a sea floor power cable in the Strait of Gibraltar. OSGWs are the dominant signal observed in shallow water (<150 m), consisting of both wind waves and swell, which are strongly modulated by the tides. We demonstrate that DAS is sensitive to sea floor pressure perturbations, though the mechanism of strain transfer to the fiber remains ambiguous. In Section 3, we describe our processing workflow. After computing OSGW NCFs, we first invert for the water depth and current velocity that describe the time-averaged OSGW dispersion relation measured along the cable. Then, we use a waveform stretching method to measure differential changes in current velocity between each pair of channels as a function of time. In Section 4, we present the result: a spatially continuous matrix of current velocity time-series across a 3-km cable segment over a period of 4.5 days. In Section 5, we compare these results to a tidal current model, and also verify that the measurements are consistent with the primitive approach of Williams et al. (2019). Then, we discuss potential sources of bias and sensitivity to depth-dependent flow, which are demonstrated with synthetic data sets. Finally, we review our findings and discuss the generalizability of the method.

2. Data

2.1. Strait of Gibraltar DAS Acquisition

We analyze OSGW in DAS data recorded on an optical fiber within a 30-km seafloor power cable running from Spain to Morocco across the Strait of Gibraltar (Figure 1). The fiber was interrogated by a chirped-pulse DAS system built by Aragon Photonics and operated by the University of Alcala (Fernandez-Ruiz et al., 2018; Pastor-Graells et al., 2016) for 22 days during October 2019, of which we use 4.5 days' continuous data between 2019-10-21 18:38:00 UTC and 2019-10-26 06:38:00 UTC. A review of the chirped-pulse DAS method is given by Fernandez-Ruiz et al. (2019). The DAS system recorded the finite strain over a 10 m gauge length every 10 m along the fiber, for a total of 2,976 channels. Throughout this paper we adopt the notational convention that strain is expressed as $1\varepsilon \equiv 1\ m/m$, such that $1n\varepsilon \equiv 10^{-9}\ m/m$. The original data was recorded at 1 kHz and later down-sampled to 1 Hz for this study.

The fiber path runs in a north-south arc immediately east of Camarinal Sill, with the northern landing site about 5 km west of Tarifa and the southern landing site due south of Tarifa on the Morocco coast near Ksar es-Seghir. The maximum water depth along the cable is ∼550 m. Over the first 8.5 km near Spain, the cable is generally buried, beyond which it is exposed at the seafloor. However, the depth of burial is poorly constrained, and several free spans (sections of cable that are hanging freely in the water column above the sea floor due to locally rough bathymetry) have been noted by the cable operators in past reconnaissance. Channels on the northern end of the cable near the Spanish coast exhibit clearer ocean wave signals than channels on the southern end of the cable, and we focus only on the northern end of the cable in this study. Due to security concerns, the cable landing locations have been omitted from Figure 1.

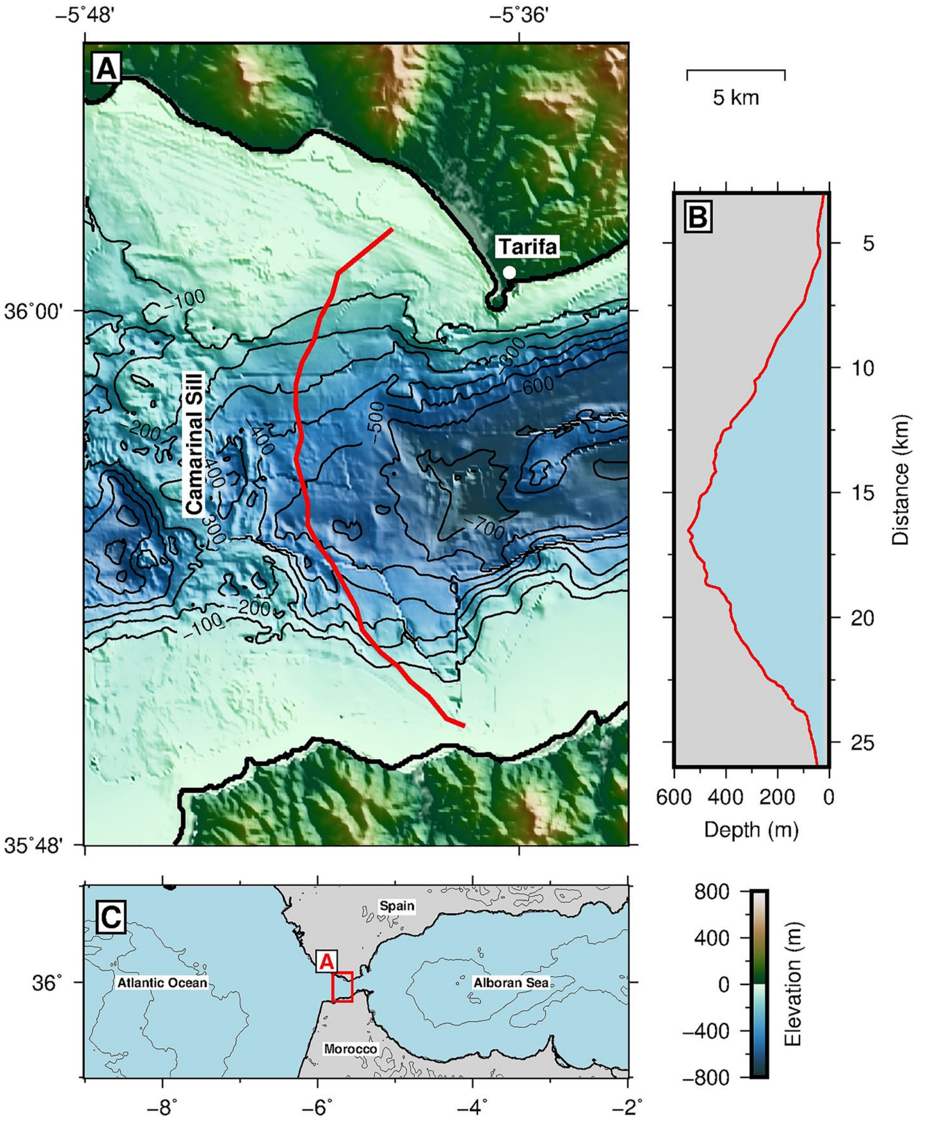

Figure 1. (a) Map of cable path across the Strait of Gibraltar, crossing between the Camarinal Sill and Tarifa Narrows. (b) Cable depth profile interpolated from the local EMODnet bathymetry grid (EMODnet Bathymetry Consortium, 2020). (c) Regional setting of (a).

2.2. OSGW Signals in DAS Data

From the Spanish shoreline to about 9-km along the cable, OSGWs are the main signal observed in the Strait of Gibraltar DAS data set, dominating the unfiltered data between 0.03 and 0.3 Hz. Waves propagating toward the shore (northeast along the cable) are significantly stronger than waves propagating away from shore (southwest along the cable). Yet, waves in both directions can be discerned by eye in the raw data (Figure 2a). The apparent phase speed is about 10 m/s, and the phase speed appears to increase with distance along the cable as the water depth increases (Figure 2a). A frequency-wavenumber (FK) transform separates the wavefield components by direction of propagation and phase speed. Figure 2b shows a FK spectrum calculated for 1 hr and 300 channels of DAS data, which demonstrates that the waves observed here generally follow the theoretical dispersion relation for OSGWs:

$$\omega^2 = gk\tanh(kh) \tag{1}$$

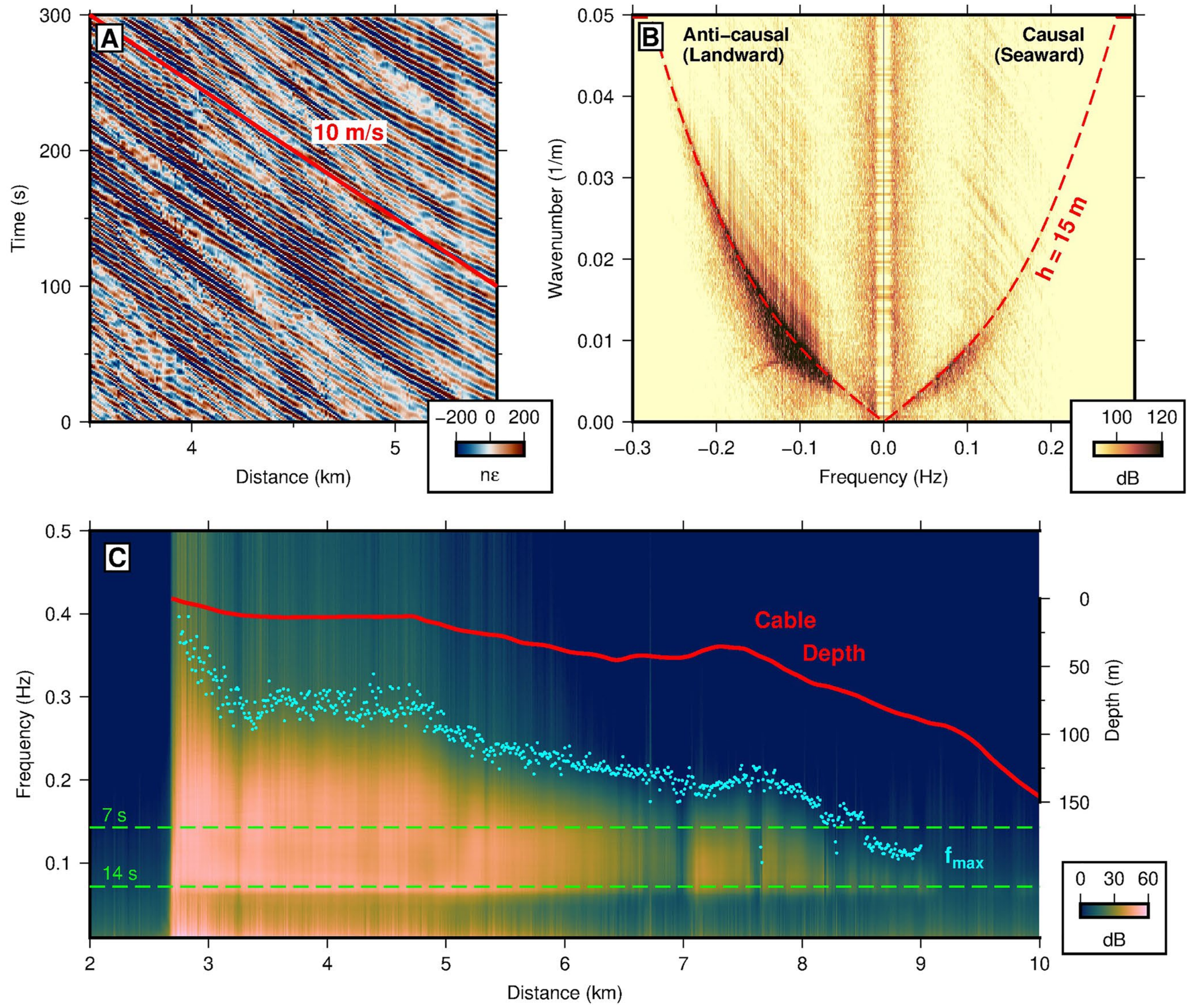

Figure 2. (a) Raw data gather showing strong ocean surface gravity wave (OSGW) propagating NE along the cable toward Tarifa, and weak OSGW propagating in the opposite direction. (b) Frequency-wavenumber spectrum of 1 hr and 300 channels of raw data, with theoretical dispersion relations for 15 m (red) water depth from Equation 1 (units are dB relative to 1 $n\varepsilon^2 \times s \times m$). (c) Median power spectral density for each channel in the first 10 km of the cable, plotted with cable depth (red) and the calculated maximum frequency (blue) (units are dB relative to 1 $n\varepsilon^2/Hz$).

where ω is angular frequency, k is angular wavenumber, h is the water depth, and g is gravitational acceleration. The FK spectrum appears broader than the curve defined by Equation 1 because waves crossing the linear array at oblique angles exhibit higher apparent velocity and smaller apparent wavenumber. To be consistent between time-domain, FK-domain, and cross-correlation representations, throughout this paper we will generally follow the convention that distance increases away from the interrogator unit (southward along the fiber from the Spanish coast) and that distances/wavenumbers are positive. Consequently, waves traveling northeast toward shore (landward) have negative time, negative frequency, and negative speed; whereas, waves traveling in the opposite direction (seaward) have positive quantities.

The median hourly power spectral densities (PSD) for the 800 channels between 2 and 10 km optical distance are plotted in Figure 2c. The cable is subaerial until the landing point at 2.7 km. Beyond 2.7 km, the OSGW spectrum is the strongest feature, consisting of two overlapping peaks between 0.05 and 0.4 Hz. The higher frequency peak represents locally generated wind waves, with a central period that decreases systematically from 6 to 8 s over the first 4–5 km, beyond which it merges with the lower frequency peak. The lower frequency peak represents swell and has a central period of about 14 s, which is invariant with water depth. While the double relationship between these two peaks mimics the double-frequency shape of the global microseism spectrum, the two peaks are unlikely to be related here. The 6–8 s peak obeys the dispersion relation for free OSGW (Figure 2b), which is incompatible with the non-linear term that the Longuet-Higgins (1950) theory of secondary microseism generation predicts at 7 s for a 14-s primary swell. Rather, the 6–8 s peak is representative of a sea state determined by local meteorological conditions. A weather station near Tarifa reported an average wind speed around 8 m/s during the experiment (Figure 3b), which corresponds to a modal period of about 6 s according to the Pierson-Moskowitz wave spectral formulation (Ochi, 1998; Pierson & Moskowitz, 1964).

The spectral amplitude of both OSGW peaks decreases with water depth, and the signal disappears shortly after 9 km distance, where the water depth is about 100 m (Figure 2c). Previous OBDAS studies have also observed decreasing depth-dependent OSGW amplitude, consistent with pressure in the linear theory of free surface gravity waves (Lindsey et al., 2019; Sladen et al., 2019; Williams et al., 2019). The pressure perturbation p_d beneath an OSGW of height ζ decays exponentially with water depth as

$$p_d(z) = \rho g \zeta \frac{\cosh(k(h+z))}{\cosh(kh)} \tag{2}$$

such that $p_d(z=-h) = \rho g \zeta / \cosh(kh)$ at the seafloor. Several localized decreases in ocean wave SNR, seen as vertical stripes in Figure 2c, are present along the cable, most notably at 3.2, 7, and 7.7 km. These could correspond to sharp bathymetric features such as channels, sections of increased cable burial depth, or free spans where the cable coupling (and thereby the nature of the measurement) differs. The OSGW bandwidth is also strongly modulated by water depth. The maximum frequency in the first 0.5 km after the landing point decreases rapidly from 0.4 to 0.28 Hz as the water depth increases to about 10 m. This rapid transformation of high-frequency wave energy in shallow water is likely enhanced by non-linear wave-wave interactions and surf-zone breaking, which have been widely observed to broaden the wave spectrum (e.g., Elgar & Guza, 1985; Herbers et al., 2003). Along the next 6 km, the maximum frequency of the higher OSGW peak follows the bathymetry closely, including a flat segment from 3.2 to 4.7 km where the shelf is level and an increase from 7 to 8 km where there is a local bathymetric high. To aid in visualizing this trend, the inflection point in the spectrum where the OSGW signal drops below the instrumental noise floor ($f_{\max}$) was measured from the second derivative of the smoothed spectrum and plotted in Figure 2c (blue dots). The minimum swell frequency of ~0.05 Hz does not change with water depth. Equation 2 implies that when the wavelength is close to the water depth ($kh \sim 2\pi$), the OSGW pressure at the seafloor vanishes. Following Crawford et al. (1991), we can then predict the maximum frequency at which OSGW are observable from Equation 1, as

$$f_{\max} = \sqrt{\frac{g}{2\pi h n}} \tag{3}$$

where $n = 2\pi/kh \sim 1$. We revisit these relationships in the following section.

Spectrograms for three individual channels (at 3, 6, and 9 km) are shown in Figure 3, along with weather and tide data from a station in Tarifa. The high-frequency wind waves are strongly tidally modulated, with both the spectral amplitude and the maximum frequency at their highest during low tide. One simple mechanism for this modulation is purely observational—an ocean-bottom instrument is closer to the surface at low tide and experiences a stronger pressure perturbation. This effect is described by Equation 3, which we evaluate with the tide gauge data from Figure 3a and plot as blue lines on Figures 3c, 3e and 3g. While the phase of the predicted modulation is consistent with the spectrogram observation and the effect diminishes similarly with depth (the tidal change in sea level is a smaller fraction of total water depth), the variation in $f_{\max}$ is underestimated by at least a factor of two. Additionally, both the bandwidth and minimum frequency of the swell are tidally modulated over the last 3 days of the experiment, which can not be described by the change in water depth alone. The phase of the modulated swell is also ahead of the wind waves by at least 45°. These features are illustrated schematically by the dashed black lines on Figure 3c. Together, these effects suggest that non-linear wave-current interaction mechanisms are necessary to describe the spatio-temporal variation of the OSGW spectrum recorded here.

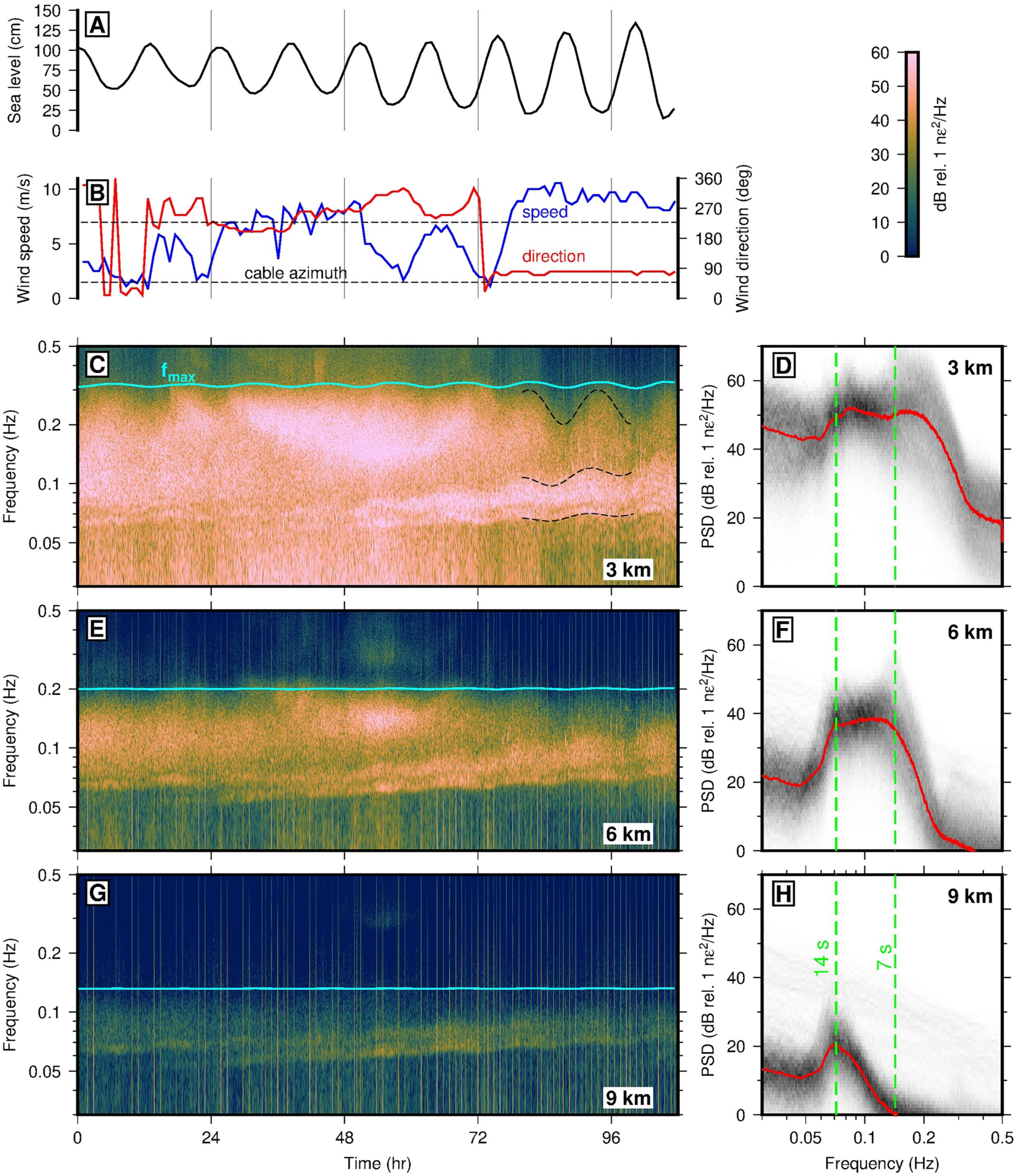

Figure 3. (a) Data from a tide gauge in Tarifa during the experiment. (b) Data from a weather station in Tarifa showing wind speed (blue), wind direction (red), and the azimuth of the cable (black). (c,e,g) Spectrograms for individual channels at 3, 6, and 9-km cable distance showing the temporal evolution of ocean wave signals. Blacked dash lines illustrate the tidal modulation of wind wave and swell energy. (d,f,h) Noise probability density functions (PDFs, normalized histograms of (c,e,g)) for the same channels with the median power spectral density plotted in red.

Another clear time-dependent feature is the enhancement of wind wave energy between 0.1 and 0.3 Hz on days 2–3 of the data set (Figure 3). The high frequency band suggests that local excitation, and not a passing storm or other distant event, is responsible. One possible explanation is that the dominant wave direction rotates into the azimuth of the cable for these 2 days. DAS measures longitudinal strain, and therefore is more sensitive to slow waves and particle motion parallel to the fiber (Martin et al., 2018). The dominant wind direction is approximately parallel to the cable for the entire experiment: for hours 0–12 and 72–108 the wind is from the northeast along the cable, and for hours 12–72 the wind is from the southwest 180° opposing (Figure 3b). Throughout all 4.5 days, the stronger component of OSGW is observed to be propagating to the northeast toward shore (Figure 2b), and the amplitude ratio of the two directional components remains approximately constant. Because the shallow cable segment is close to the coast on the northeast side (Figure 1), this suggests that waves propagating southwest away from shore are primarily the result of coastal reflection, and, as the coastal reflection coefficient does not vary in time, changes in the point spectrum (e.g., Figure 3c) must result from varying wave conditions in the Strait to the south. The 3–6 km cable segment will observe waves generated south of this segment by the southwesterly wind on days 2–3, whereas waves generated in the same location by the northeasterly wind on other days will propagate away from the array. However, the wind speed is significantly higher on days 4–5 when the wind wave signal is weakest. Quantitative modeling would be necessary to definitively identify the cause of this high-frequency wave event.

2.3. The Nature of the Measurement

The measurement principle of DAS when applied as a seismometer relies on the assumption that changes in optical path length in the fiber are dominated by deformations of the physical fiber length, that is, elastic strains. However, DAS is sensitive to temperature as well—the combined effects of temperature on the index of refraction and thermal expansion equate to an equivalent elastic strain of 1 nε per 10 mK. At seismic frequencies, thermal signals can be neglected (Lindsey et al., 2020), but at tidal frequencies and in submarine environments with significant temperature gradients, temperature effects may dominate the DAS measurement (Ide et al., 2021). Throughout the experiment, observed OSGW amplitudes are on the order of 100 nε between 3 and 6 km where the average water depth is about 40 m. This equates to a temperature signal of order 1 K, which is unreasonable given typical stratification and OSGW displacement near the seafloor. The effect of temperature can therefore be neglected here.

Having established that OSGW observations in OBDAS data from the Strait of Gibraltar represent elastic strain of the fiber element within the cable, we must consider how the DAS measurement is related to OSGW physical quantities. As described above, Equation 3 describes the maximum frequency at which seafloor observation of OSGW pressure is possible. Plotting the observations of $f_{\max}^2$ for each channel from Figure 2c against the bathymetric prediction $\frac{g}{2\pi h}$, Figure 4a shows that $n \approx 1$ over the 3.2–9 km cable segment, meaning that frequency band of OBDAS strain scales consistently with pressure. The only exception is in the 0.5 km closest to shore in <10 m water depth, where $n > 2$, meaning that the observed $f_{\max}$ is lower than predicted by the water depth. This is likely a result of the instrumental noise floor being higher for the individual channels in the surf zone which are saturated with strong wave energy, so the observed $f_{\max}$ corner appears lower even though the wave energy is higher.

On conventional OBS, surface gravity waves are observed on both the pressure gauge and seismometers, indicating that the hydrodynamic pressure from gravity waves is large enough to deflect the seafloor—a likely mechanism by which OSGW pressure is related to OBDAS strain. The measure of this deflection is termed seafloor compliance (the ratio of displacement to applied stress, $\xi = u/\tau_{zz}$), and has been used for both OSGW in shallow water (Yamamoto & Torii, 1986) and infragravity waves in deep water (Crawford et al., 1991) to constrain the elastic structure of oceanic lithosphere. OBDAS measures the average horizontal strain over a gauge length $\left(\varepsilon_{xx}^{L} \approx \frac{1}{L}\int_{-L/2}^{L/2} \varepsilon_{xx}\, dx\right)$, which is close to the horizontal strain at a point when the wavelength is much longer than the gauge length ($\varepsilon_{xx}^{L} \approx \varepsilon_{xx} = \partial_x u_x = k u_x$). Consequently, the relationship between the applied pressure at the seafloor from OSGW and the horizontal strain observed by OBDAS is the normalized horizontal compliance

$$\eta_x = k\frac{u_x}{\tau_{zz}} = \frac{\varepsilon_{xx}}{p_d} = \frac{\lambda + 2\mu}{2\mu(\lambda + \mu)} \tag{4}$$

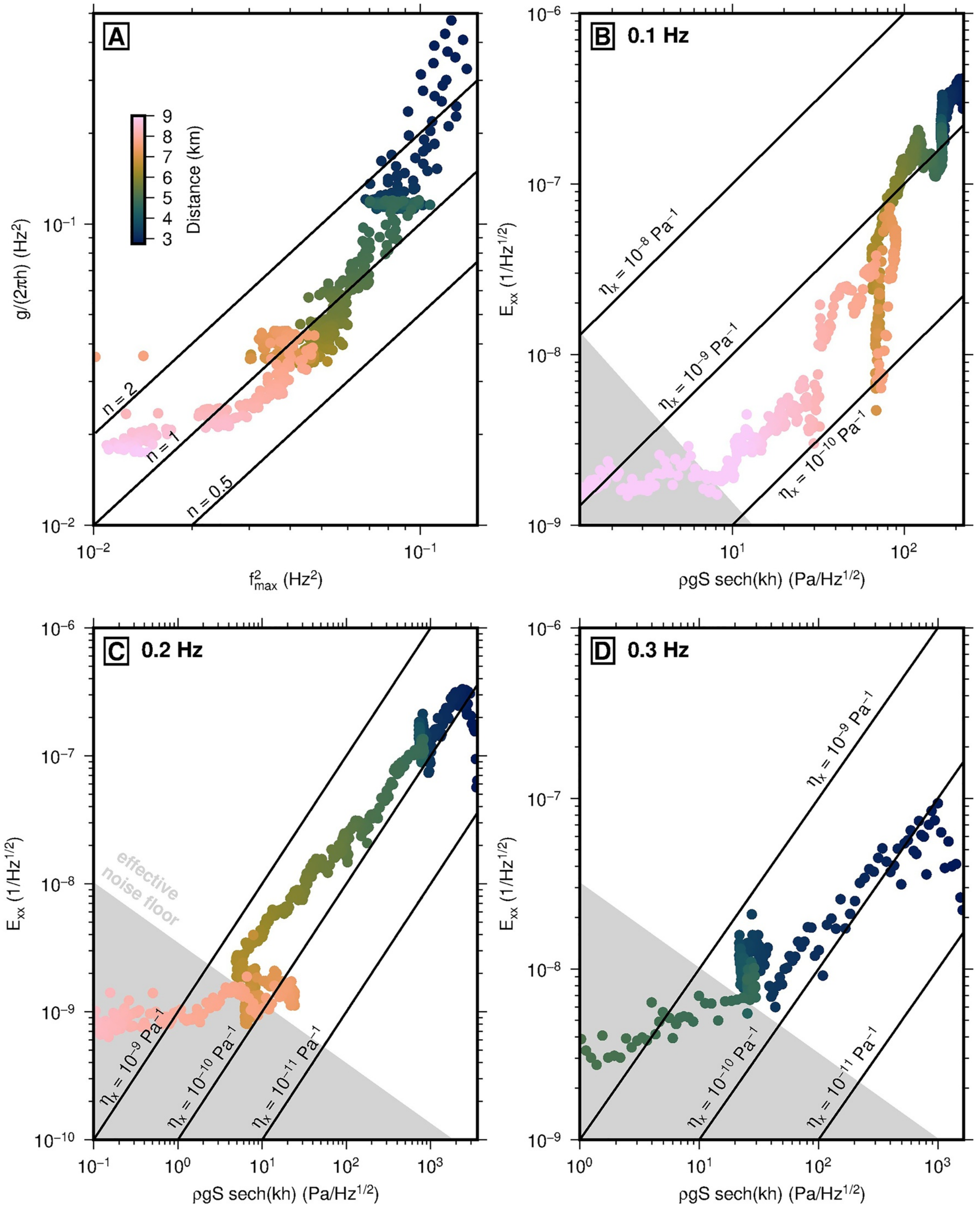

Figure 4. (a) Scaling between water depth and the maximum frequency of ocean surface gravity wave (OSGW) (f_{max}) according to Equation 3. Each point represents an individual channel, colored by distance along the cable. (b) Scaling between observed strain amplitude spectrum (E_{xx}) and modeled seafloor pressure spectrum ($\rho g S/\cosh(kh)$) according to Equation 5. (c, d) Same as (b) but for 0.2 and 0.3 Hz respectively. The point where OSGW signals fall below the instrumental noise floor is indicated with gray shading.

where (λ, μ) are the Lamé parameters in the linearized solution for a uniform elastic half-space (Crawford, 2004). Normalized horizontal compliance at the high frequencies of wind waves considered here has not yet been studied and is strongly dependent on the V_P/V_S ratio of shallow sediments, which can vary by an order of magnitude. At 0.01 Hz, $\eta_x \sim 10^{-10}$ to 10^{-9} Pa^{-1} (Doran & Laske, 2016). At 0.1 Hz, plausible values of normalized horizontal compliance could range from 10^{-9} at $V_P/V_S = 2$ to 10^{-7} Pa^{-1} at $V_P/V_S = 20$, using the method of Crawford et al. (1991) with a generic crustal velocity model and varying V_S in the top 20 m.

We compare the OBDAS strain amplitude spectrum ($E_{xx} = |\mathcal{F}[\varepsilon_{xx}]|$, where $\mathcal{F}$ denotes the Fourier transform) with the expected scaling of seafloor pressure at three frequencies in Figures 4b–4d for each channel between the landing point and 9 km. Combining the pressure-depth scaling of OSGW (Equation 2) with the definition of compliance (Equation 4), we obtain

$$E_{xx}(\omega) = \eta_x \left(\frac{\rho g S(\omega)}{\cosh(kh)} \right) \tag{5}$$

where $S = |\mathcal{F}[\zeta]|$ is the Pierson and Moskowitz (1964) spectrum for wave height (evaluated for a modal period of 6 s and converted into units of $\mathrm{m/Hz}^{1/2}$). While Equation 2 is derived under the assumption of a rigid seafloor, the relative contribution of seafloor deformation to the ocean-bottom pressure field is small and can be neglected for reasonable values of compliance (Latychev & Edwards, 2003; Yamamoto & Torii, 1986). Note that the pressure-depth scaling in each panel of Figures 4b–4d differs because $k = k(\omega, h)$ following Equation 1. The near-horizontal tail in the bottom-left corner of each panel represents instrument noise at channels where the OSGW signal is too weak to be observed, as delineated by $f_{\max}$ in Figure 2c.

At 0.2 and 0.3 Hz (Figures 4c and 4d), the observed strain generally follows the linear functional form predicted by compliance theory (Equation 5), which offers further evidence that OBDAS is observing a quantity proportional to OSGW dynamic pressure. The value of normalized horizontal compliance is approximately 10^{-10} Pa^{-1} at both 0.2 and 0.3 Hz, which is 10–1,000 times too small to be physically plausible. Laboratory experiments have demonstrated that the amplitude response of DAS (the difference between observed and applied strain) is flat across the range of frequencies examined here, though field experiments have shown that the design or installation properties of the cable may affect the apparent amplitude response by mediating strain transfer to the fiber (Lindsey et al., 2020; Paitz et al., 2021). Submarine cables often include a gel layer designed specifically to protect the interior components from strain during deployment, so the strain experienced by the fiber may be much smaller than the exterior deformation of the seafloor. A second possible explanation for the amplitude discrepancy relates to the use of a point spectrum for sea surface height. Realistic wind-driven ocean wave fields exhibit a non-isotropic directional spectrum, meaning that the horizontal displacement spectrum of the seafloor from OSGW compliance is azimuthally dependent. In previous analysis of OBS horizontal compliance data, Doran and Laske (2016) rotated the horizontal seismometer components into the direction that maximized coherence with the pressure gauge. Because DAS only measures one wavefield component, such a correction is impossible, and the probability that the cable is oriented away from the principal wave direction is high. Consequently the observed horizontal strain is only a fraction of the total seafloor deformation that would be predicted from a point spectrum of sea surface height. Finally, cable burial could explain the low strain amplitude, because compliant deformation under OSGW loading decays exponentially with depth below the seafloor (Crawford, 2004; Crawford et al., 1991). The depth of burial has not been mapped for this cable, so the effect of burial cannot be evaluated. Notably, Lior et al. (2021) found that earthquake strain amplitudes observed on an unburied, light weight seafloor cable were consistent with nearby seismometer records after accounting for the direction of wave propagation.

At 0.1 Hz (Figure 4b), the observed strain is not consistent with the expected pressure-depth scaling from Equation 5. The values of compliance shown in Figure 4b are less realistic because the wave energy at 0.1 Hz is dominated by swell, which is not adequately described by the Pierson and Moskowitz (1964) spectrum. However, we still expect to observe the same linear scaling. Instead, the necessary value of η_x increases by a factor of 10 from deep water at 9 km to the landing point at 2.7 km, indicating that, after accounting for the difference in water depth, the amplitude systematically increases toward the coast. This increase in apparent amplitude may represent a change in the cable-seafloor elastic coupling or burial depth beyond ~6 km cable distance. Because the wavelength at 0.1 Hz is long compared to the water depth ($\lambda \approx 100$ m), growth of swell amplitude due to shoaling on the sloping bathymetry may also contribute.

Alternatively, if the cable is unburied or poorly coupled to seafloor sediments, the observed relationship between OSGW dynamic pressure and OBDAS strain may result from direct pressure loading of the cable and not compliant deformation of the seafloor. In this case, a local change in pressure exerts an isotropic radial stress on the cable, resulting in longitudinal strain according to the Poisson's ratio of the cable itself. Mecozzi et al. (2021) considered the effect of direct pressure loading to account for ocean swell observations on Google's transoceanic Curie cable and estimated a sensitivity of $\frac{\varepsilon}{\Delta p} \approx 3 \times 10^{-9}$ Pa^{-1}. The result of Mecozzi et al. (2021) is also consistent with the transfer function between OBDAS and a collocated pressure gauge reported by Matsumotu et al. (2021) for high-frequency hydroacoustic waves. This value is about 10 times too large to account for the observed strain here and is of similar magnitude to the normalized horizontal compliance discussed above. Because the deep sea Curie cable is a telecommunications cable (centimeter-scale diameter and light-weight construction), whereas the data analyzed here is from a power cable (decimeter-scale diameter with three insulated metal conductors), differences in construction could account for a reduction in Poisson's ratio and account for our observation of $\frac{\varepsilon_{xx}}{p_d} \approx 10^{-10}$ Pa^{-1}.

In summary, OBDAS is sensitive to the hydrodynamic pressure from OSGW, but the mechanism by which seafloor pressure is transferred to the cable remains ambiguous. Further calibration experiments are needed to constrain the sensitivity of OBDAS, ideally including in-situ measurements of ocean-bottom pressure and directional wave spectra. Importantly, both mechanisms of pressure-to-strain conversion considered above have a flat phase response. Therefore OBDAS data can be treated as ocean-bottom pressure data for the purposes of ambient noise interferometry in the analysis that follows.

3. Methods

3.1. OSGW Interferometry

The OSGW field measured at any point in time and space represents the superposition of waves generated by a distribution of diverse sources. Such measurements are not repeatable, but OSGW observations appear coherent across a broad range of space and time scales (Webb, 1986; Webb et al., 1991) both because the individual wavefield components propagate deterministically in a shared continuum and because the sources tend to obey quantifiable statistics (Ochi, 1998). These same properties are observed for ambient seismic and ocean acoustic noise. Provided the wavefield is sufficiently diffuse, cross-correlation (interferometry) of ambient noise time-series recorded at two points yields an empirical approximation of the Green's function for waves propagating between those points (e.g., Brown and Lu, 2016; Godin, Zabotin, et al., 2014):

$$x_{AB}(t) = \int_{-\infty}^{\infty} u_A(\tau) u_B(t+\tau) d\tau \propto d(t) * [g(B|A,t) + g(A|B,-t)] \tag{6}$$

Here, x_{AB} is the NCF between the wavefield u recorded at points A and B, and d collapses the source terms of the ambient wavefield and should approximate a delta function. The Green's function terms $g(B|A,\ t)$ and $g(A|B,\ -t)$ represent wave propagation along reciprocal ray paths between A and B. When applied to seismic waves in the solid earth, the reciprocity relation dictates that $g(B|A,\ t) = g(A|B,\ t)$, and the NCF is symmetric. However, for waves in a moving medium, such as OSGW propagating in a current, $g(B|A,\ t) \neq g(A|B,\ t)$; rather, $g(B|A,t) = \tilde{g}(A|B,t)$, where $\tilde{g}$ denotes the Green's function in a medium where the flow is reversed (Godin, 2006). The flow velocity directly dictates the degree of non-reciprocity, and thereby the asymmetry of the NCF (Equation 6). This property was used by Godin, Brown, et al. (2014) with acoustic interferometry to measure flow between hydrophones, and we can exploit it again here to map the spatio-temporal variation of current speed along the Strait of Gibraltar OBDAS array.

To compute cross-correlations, we select only channels 300–600 where the OSGW energy is strong, broadband, and spatially smooth (no sharp changes in cable properties), and divide the 108-hr data set into 215 1-hr subsets overlapping by 50%. For each hour, we apply FK filters with a pass-band of $c = f/k \in [2,\ 50]$ m/s and $c \in [-50,\ -2]$ m/s to separate the data into separate workflows for positive and negative wavespeeds (causal and anti-causal time lags) and eliminate all non-OSGW signals. The rest of the processing closely follows the standard workflow proposed by Bensen et al. (2007): the filtered, hourly data subsets are divided further into 8.5-min (512 sample) windows, spectral normalization is applied to each channel over $f \in [0.01,\ 0.5]$ Hz, each pair of channels is cross-correlated in the frequency domain for a total of $N(N+1)/2 = 45{,}150$ pairs, and the 8.5-min windows are normalized and stacked to form hourly NCFs. The result is $215 \times 45{,}150$ hourly NCFs for each of the causal and anti-causal wavefield components.

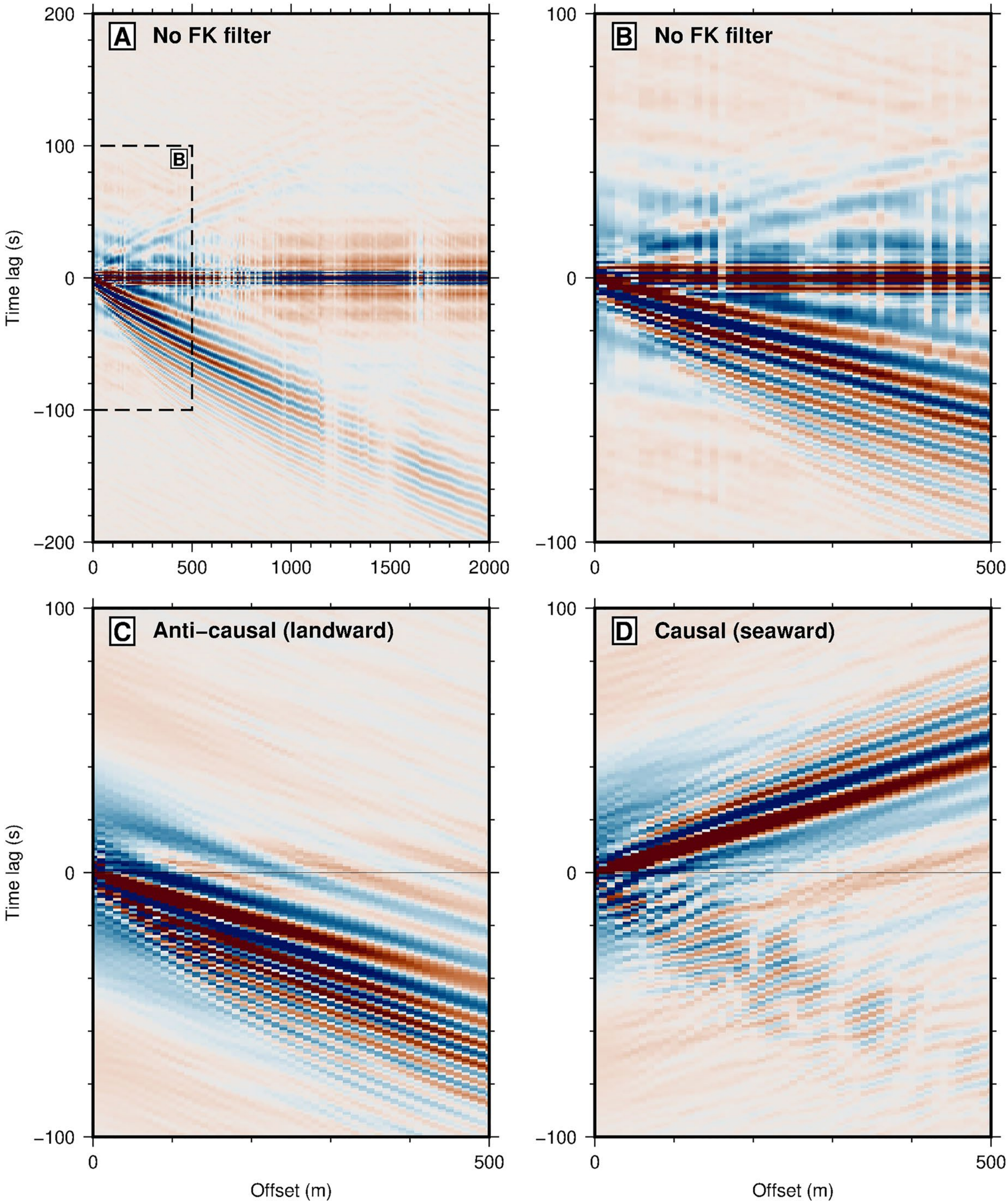

Figure 5. Example virtual source gather formed by cross-correlating channel 350 (at 3.5 km) with all channels between 350 and 550 (5.5 km). (a) Virtual source gather computed without frequency-wavenumber (FK) filtering, and (b) same as (a) but zoomed in to the first 500 m offset. (c, d) Same as (b) but with FK filtering selecting negative (landward propagating) speeds and positive (seaward propagating) speeds, respectively. Amplitude is normalized to arbitrary units during spectral whitening (0.01–0.5 Hz).

An example virtual source gather (the cross-correlation of one channel with each adjacent channel in a subarray) stacked over the complete 4.5 days data set is shown in Figure 5, illustrating how the interferometric processing transforms a random wavefield (as in Figure 2a) into an organized wavefield, with a single OSGW packet propagating away from a point source. Figures 5a and 5b show the result of processing if the FK filtering step

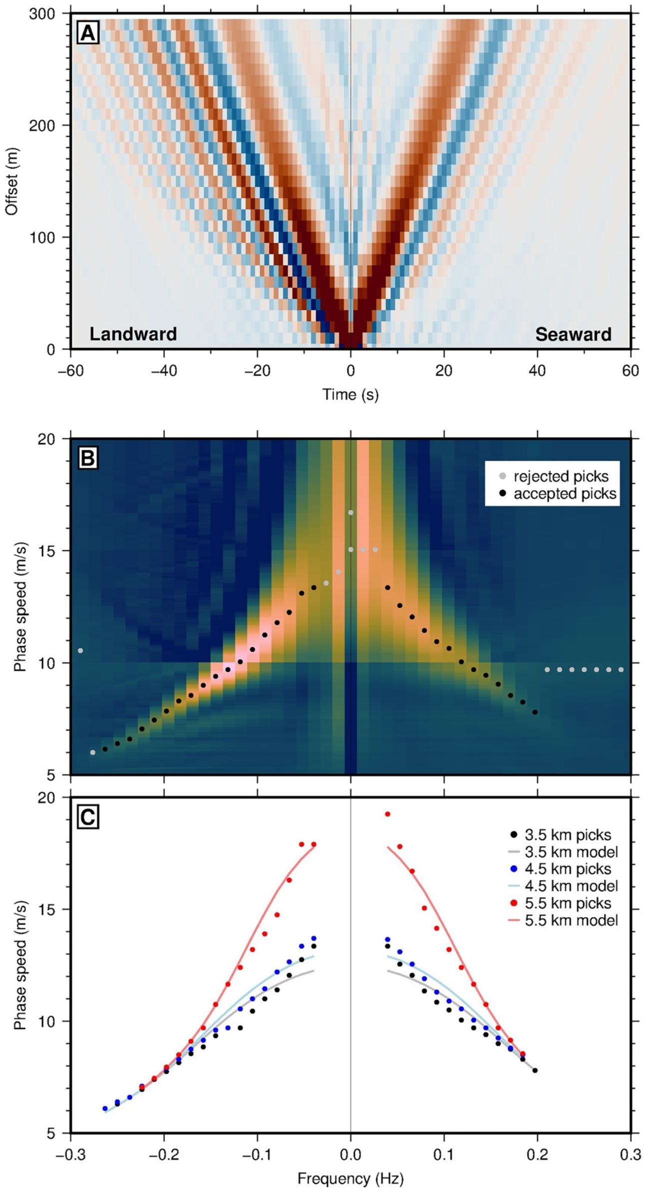

Figure 6. Composite images combining FK-separated cross-correlations showing: (a) example 300-m virtual source gather used in dispersion analysis; (b) dispersion images computed from (a) with picks in each frequency bin; and (c) example dispersion picks and best-fitting dispersion curve at three locations along the cable. Although spectral whitening was applied over 0.01–0.5 Hz, reliable dispersion picks are only made between 0.03 and 0.27 Hz (anti-causal) and 0.03–0.2 Hz (causal).

is omitted, while Figures 5c and 5d show the separated results. Without FK filtering, NCFs are imbalanced between causal and anti-causal time lags, with much stronger wave energy propagating toward the shore as observed in the raw data. Spectral whitening is applied before cross-correlation in order to boost the contribution from weaker frequencies that still have coherent phase information, which has an unbalanced effect if the raw data is dominated by a single directional component. By separating the causal and anti-causal components into the separate workflows, the high frequency energy propagating away from the shore is enhanced. Instrumental noise that concentrates at zero lag in cross-correlations can also be mitigated by FK filtering the raw data. However, FK filtering does introduce some spatial smoothing, which may result in loss of resolution, and sharp features in the data such as poorly coupled channels can introduce ringing artifacts if not treated carefully.

3.2. Current Measurement

In order to measure current velocity, we compare NCFs for the two directional wave components and fit the non-reciprocity with a dispersion relation that describes OSGW propagating in a current. In the absence of a current, the OSGW problem reduces to the 2D Helmholtz equation, which can be expressed either in terms of wave height or ocean-bottom pressure (see Brown and Lu, 2016; Godin, Zabotin, et al., 2014 for a detailed derivation). For $k(\omega) r \gg 1$, the Green's function solution for pressure ($G(r,\omega) = \mathcal{F}[g(r,t)]$) is then

$$G(r,\omega) \propto H_0^{(1)}(k(\omega)r) \approx \sqrt{\frac{2}{\pi k(\omega)r}}\, e^{i(k(\omega)r-\pi/4)}. \tag{7}$$

The term above is $k(\omega)r = \frac{\omega r}{c_0(\omega)}$, with the phase speed $c_0(\omega) = \frac{\omega}{k} = \pm\sqrt{\frac{g}{k}\tanh kh}$ defined by Equation 1. For small currents, we can modify this solution by perturbing the dispersion relation. In the case of a uniform current $U(z) = U_m$, the dispersion relation is simply $c(\omega, U_m) = c_0(\omega) + U_m$. Note that c_0 is negative for one directional component, so the addition of U_m is non-reciprocal—a Doppler shift.

Although the signal-to-noise ratio (SNR) of computed OSGW NCFs is high when stacked over the complete 4.5 days experiment (Figure 5), the SNR of hourly NCFs is much lower, especially for the causal (seaward) directional component. In order to exploit the coherent phase information over a broad frequency band in the 4.5-day stack, we propose a two-step approach to current measurement. First, we measure phase speed dispersion for the complete stack and solve for the best-fitting dispersion relation, which includes the water depth and mean current as a function of distance along the cable. Second, we measure the difference in current velocity at each hour relative to the mean using a modified form of the popular stretching method from seismology.

3.2.1. Mean State Inversion

We divide the array into overlapping 300 m (30 channel) subarrays and form virtual source gathers for each of the two directional components (Figure 6a). The subarray aperture is chosen to maximize the bandwidth of dispersion picks while minimizing the effect of smoothing the recovered bathymetry profile. Due to attenuation, the highest-frequency OSGW energy (above 0.2 Hz) is only evident in NCFs with offset less than about 100 m, so the subarray must begin close to the virtual source. Conversely, the dispersion relation for OSGWs results in fast move-out of low-frequency energy, so the beamforming resolution is poor for offsets shorter than about 100 m. For the case of the Gibraltar data set, bathymetric features along the cable path such as the sharp shelf break at 4.7 km and two bumps around 5.5 km cannot be recovered if the subarray is larger than 300 m.

We then apply beamforming and a Fourier transform to measure phase speed dispersion as a function of frequency for each of the two directional components:

$$B_i\left(\omega, c'\right) = \sum_{j=i}^{i+N} X_{ij}(\omega) e^{\frac{-i\omega r_{ij}}{c'}}, \tag{8}$$

where $c' \in [5, 20]$ m/s, $X_{ij}(\omega) = \mathcal{F}\left[x_{ij}(t)\right]$, and i, j are channel numbers. The resulting dispersion images $B_i(\omega, c')$ for each subarray can be interpreted as a likelihood map for the phase speed in each frequency bin. We take the phase speed as $\underset{c'}{\operatorname{argmax}}\, B_i\,(\omega,\, c')$ for each frequency $\geq$0.03 Hz, and manually set a threshold value of B to exclude spurious picks at high frequencies, as illustrated in Figure 6b. Combining the set of dispersion measurements for the two independent directional components, we use a non-linear least squares (Levenberg-Marquardt) solver to find the values of (h, U_m) that minimize the misfit with the dispersion relation for uniform flow across both positive and negative frequencies (Figure 6c):

$$c\,(\omega, U_m) = \pm\sqrt{\frac{g}{k}\tanh\,(kh)} + U_m \tag{9}$$

Across the complete 3-km cable segment (Figure, 7a), the maximum frequency of dispersion picks is about 0.2 Hz for the causal component, whereas the anti-causal component includes picks up to 0.3 Hz in shallow water, decreasing with depth following the same trend as $f_{\max}$ in Figure 2c. Even though the phase speed is more sensitive to water depth than current velocity (a typical value of U_m is < 0.5 m/s), incorporating picks on both positive and negative frequency sides of the dispersion relation into the inversion mitigates the covariance between current speed and water depth, as a change in current speed is an asymmetric shift. In principle, the same procedure can be applied for any wave-current model parameterization, such as for depth-dependent flow.

3.2.2. Stretching

The stretching method is a common approach to measuring time-dependent changes in the velocity of coda waves from earthquakes or ambient noise cross-correlations (Sens-Schönfelder & Wegler, 2006). Because perturbations from environmental processes are small relative to the absolute speed of seismic waves ($\ll$1%), the associated change in travel-time is difficult to measure. The stretching method solves for differential changes in velocity by warping the waveform measured at one time until it matches a reference waveform, thereby incorporating all the phase information from a complete trace into the search for a single parameter. For the case of OSGW interferometry, the relative velocity perturbations from ocean currents can be quite large (up to 10% at high frequencies), but the ocean environment evolves rapidly relative to the time scale of convergence of NCFs. Consequently the SNR for a single hourly NCF may be too low to make independent phase speed measurements at a sufficiently broad range of frequencies to constrain the dispersion relation, as done above. The stretching method leverages the higher SNR of the reference trace to extract the coherent phase information contained in individual traces even when SNR is low. The original method uses a linear stretching factor to model the response of scattered, non-dispersive waves to a homogeneous velocity change; the modified stretching method proposed here uses a frequency-dependent stretching factor to model the response of ballistic, dispersive waves to a non-reciprocal velocity change.

For each NCF pair, we define the reference trace as the stack of all hourly NCFs across the complete 4.5 days data set because this maximizes the SNR and we already know the dispersion relation for the mean state. Following from Equations 6 and 7, the reference trace can be expressed as $X_{ij}^0(\omega) = A^0(\omega)e^{\frac{i\omega r_{ij}}{c_m(\omega)}}$, where $c_m = c_0 + U_m$ as above. Similarly, any given hourly NCF is $X_{ij}^n(\omega) = A^n(\omega)e^{\frac{i\omega r_{ij}}{c(\omega,U)}}$, where $c = c_0 + U$. Assuming that $A^0(\omega)$ and $A^n(\omega)$ are similar, we can write the hourly NCF in terms of the reference trace:

$$X_{ij}^n(\omega) \approx X_{ij}^0(\omega)e^{i\omega r_{ij}\delta s} = X_{ij}^{\delta s}(\omega, U), \quad \text{where}\ \delta s(\omega, U) = \frac{1}{c(\omega, U)} - \frac{1}{c_m(\omega)} \tag{10}$$

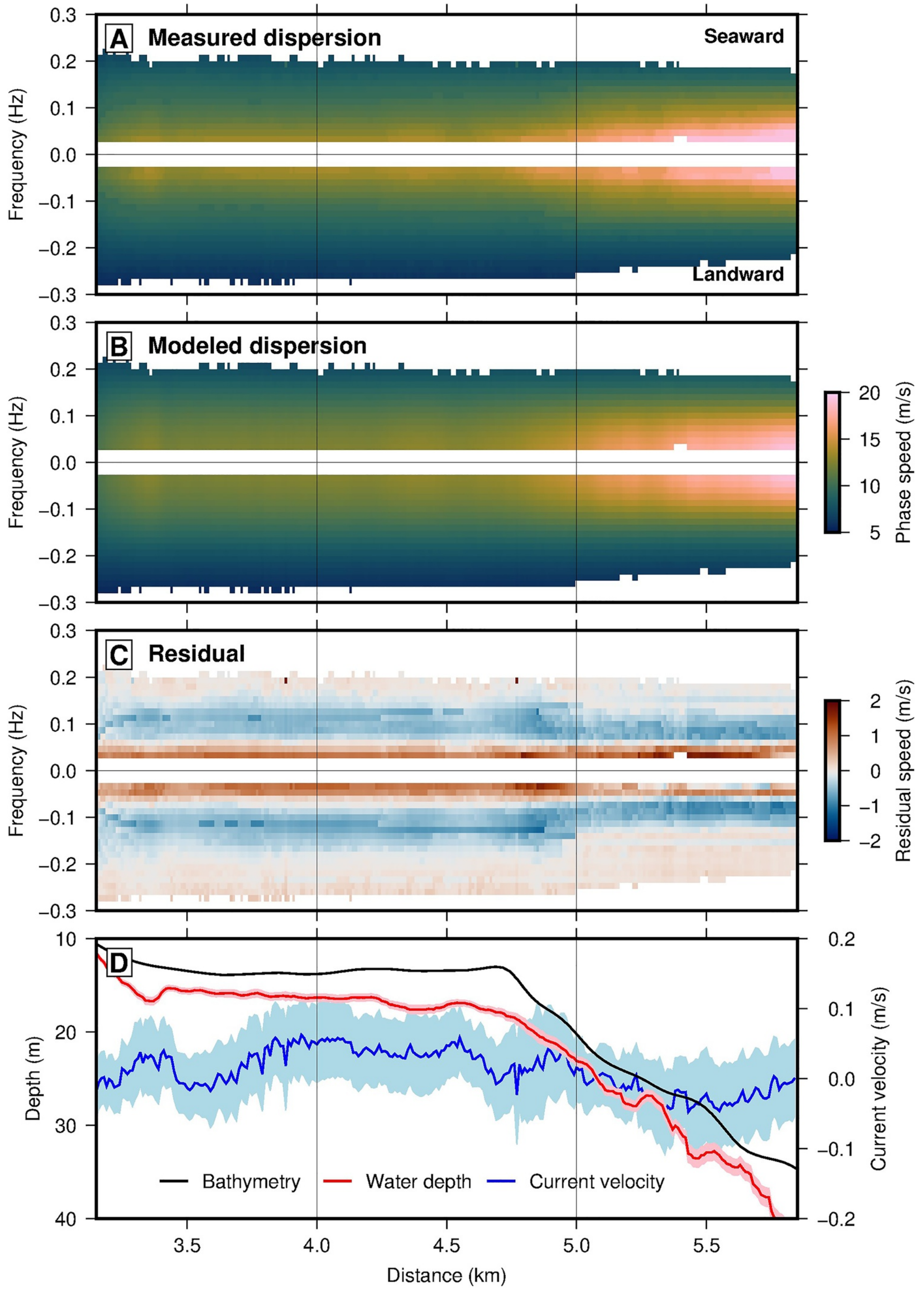

Figure 7. Mean-state inversion results: (a) dispersion picks for all subarrays along the cable; (b) modeled (best-fitting) dispersion curves; (c) difference between (a and b); and (c) inverted model parameters water depth (h) and flow velocity (U) plotted with 1σ error bars.

This defines a frequency-dependent stretching factor $\delta s(\omega, U)$, which can transform the phase spectrum of the reference trace X_{ij}^{0} into any given hourly NCF X_{ij}^{n} (Figures 8a and 8c).

Because there is only one unknown parameter, U, we can directly invert for the flow velocity, and a simple grid search is sufficiently computationally efficient. We pre-compute a dictionary of stretched reference traces

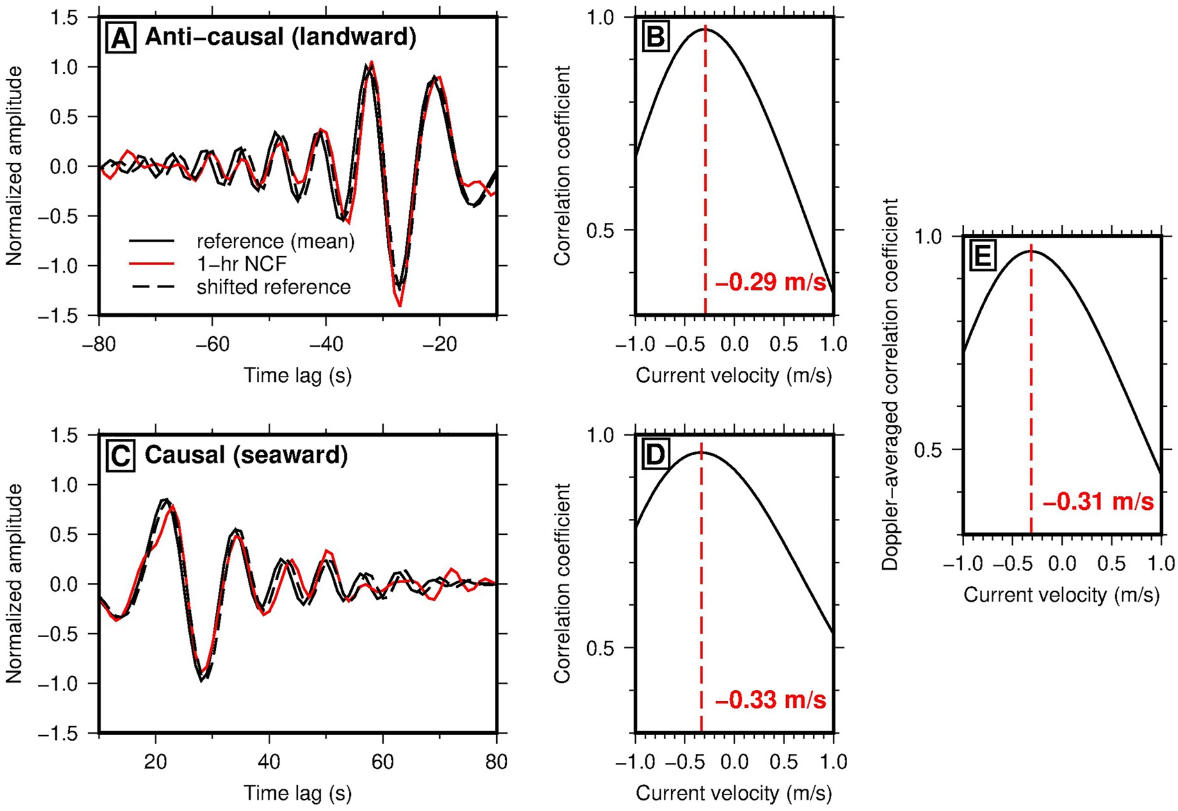

Figure 8. Example of the modified stretching method for the noise correlation functions (NCF) of a single pair of channels at one point in time, showing: (a, c) the 1-hr stacked NCF, the reference NCF, and the shifted reference NCF that maximizes the correlation coefficient with the 1-hr NCF for the anti-causal and causal sides respectively; (b, d) the correlation coefficient as a function of current velocity for the NCFs in (a, c); (e) the doppler-averaged correlation coefficient from (b, d).

$x_{ij}^{\delta s}(t,U) = \mathcal{F}^{-1}\left[X_{ij}^{0}(\omega)e^{i\omega r_{ij}\delta s(\omega,U)}\right]$, $U \in [-1, 1]$, then compute the correlation coefficient for each hourly NCF with each stretched reference trace:

$$CC_{ij}^{n}(U) = \frac{\int_{t_1}^{t_2} x_{ij}^{n}(t)x_{ij}^{\delta s}(t,U)dt}{\sqrt{\int_{t_1}^{t_2} x_{ij}^{n\,2}(t)dt \int_{t_1}^{t_2} x_{ij}^{\delta s 2}(t)dt}} \tag{11}$$

where $t_1 = r_{ij}/c_g(\omega_2)$ and $t_2 = r_{ij}/c_g(\omega_1)$ define the travel-time window containing the ballistic wave. Here, $c_g(\omega) = \frac{c_0(\omega)}{2}\left(1 + \frac{2kh}{\sinh(2kh)}\right)$ is the OSGW group velocity, which is evaluated at the minimum and maximum frequencies of interest (ω_1, ω_2). The values $(\omega_1, \omega_2) = 2\pi(0.03, 0.3)$ are chosen to ensure that the full available bandwidth is included in the computation of $CC_{ij}^{n}(U)$ for all water depths. For this data set, although we start with spectral normalization over the band 0.01–0.5 Hz, the resulting NCFs only exhibit coherent OSGW signals over 0.03–0.3 Hz (e.g., Figure 7). In a data set with greater variations in bathymetry along the cable path, the window could be set adaptively based on the coherence between traces instead, or using the theoretical maximum observable frequency $f_{\max}(h)$ (Equation 3). The result is an array of $CC(U)$ for each of the causal and anti-causal components (Figures 8b, 8d and 8e), which can be interpreted as a likelihood function for U. This formulation neglects the effect of temporal variations in water depth on OSGW dispersion, which may be significant in shallow water. A change in h results in a reciprocal (symmetric) change in the phase speed (Equation 9), which can be removed by combining the causal and anti-causal sides into a joint inversion (see Section 5.1.). So, we average the two $CC_{ij}^{n}(U)$ into a single Doppler-averaged correlation coefficient (DACC) and take the maximum value as the solution. Generally, the peak values of the DACC are >0.95 for all traces and all time windows.

The time-lapse evolution of a single representative NCF pair separated by 300 m is shown in Figures 9a and 9b, exhibiting clear periodicity in travel-times at the M2 tidal period. Applying the modified stretching method to

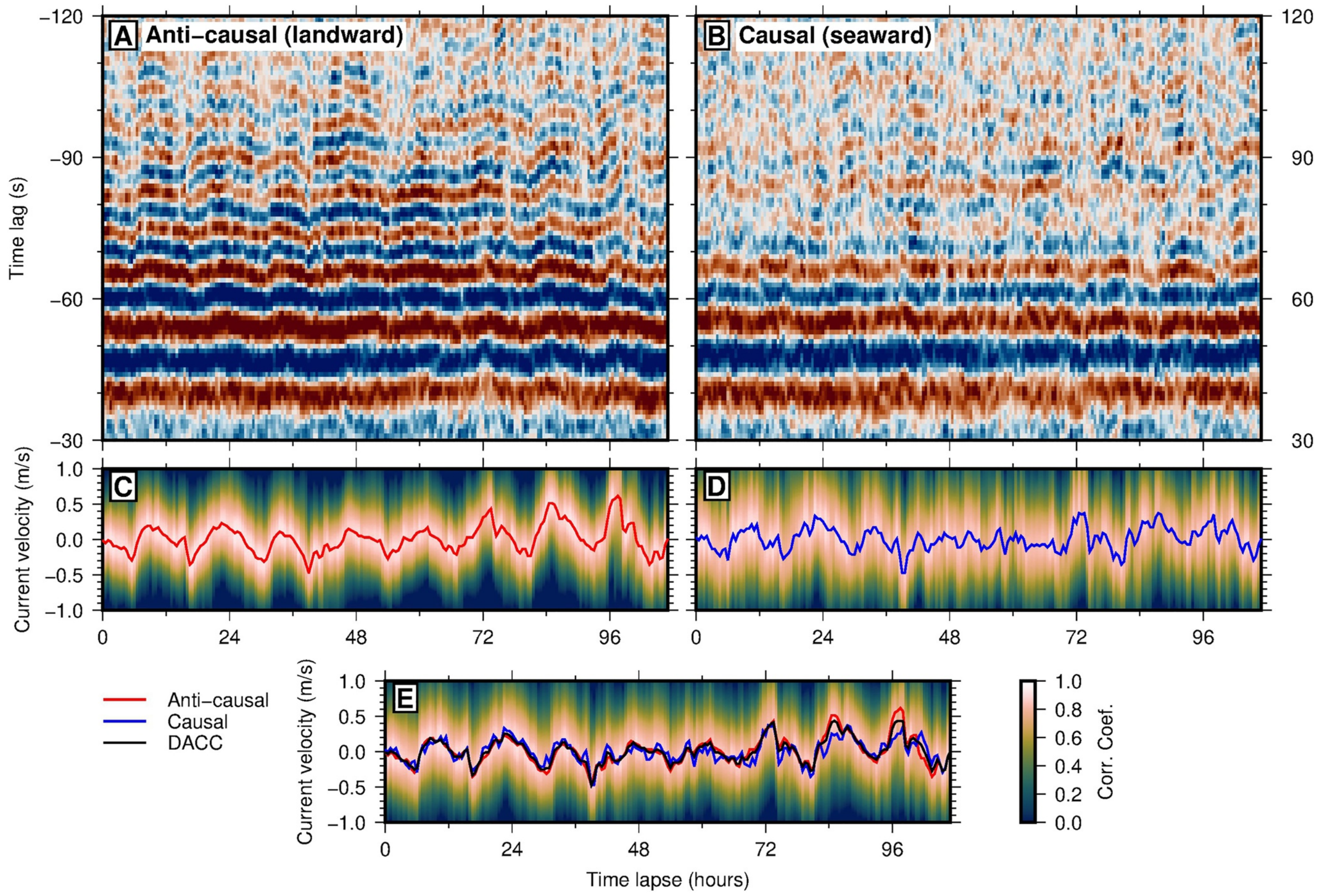

Figure 9. Results of applying the modified stretching method to example noise correlation functions (NCF) for a single pair of channels across all 1-hr windows. (a, b) Time-lapse gathers for the anti-causal and causal sides respectively showing time-dependent changes in the arrival time of ocean surface gravity waves. Note that the relative amplitude of NCFs is not preserved between the causal and anti-causal sides due to the separate processing workflows (Figure 5). (c, d) Correlation coefficients computed from stretching (a, b) over a range of velocities, with the velocity that maximizes the correlation coefficient with the reference NCF indicated in red and blue. (e) The Doppler-averaged correlation coefficient (DACC) computed from (c, d) superimposed with the optimal velocities from (c, d) and the DACC pick in black.

each 1-hr window in the 4.5-day time-series produces a matrix of correlation coefficients for each candidate U at each hour. The selected U values for the anti-causal side (red) show a clear tidal signal with a reasonable amplitude of about 0.5 m/s (Figure 9c). The selected values for the causal side (blue) appear much noisier, owing to the lesser SNR of the NCFs for this wavefield component, but still show a tidal signal (Figure 9d). When superimposed it is clear that even though the causal side measurement (Figure 9d) appears much noisier, it is actually broadly consistent with the anti-causal side measurement. This is significant because the FK pre-processing and parallel workflows ensure that these measurements are independent. Combining Figures 9c and 9d into the DACC and making a joint estimate of U (black), results in a current velocity time-series in between the two one-sided estimates (Figure 9e).

4. Results

4.1. Depth Profile

The results of subarray beamforming to invert for the mean state are shown in Figure 7. Dispersion picks (Figure 7a) are symmetric for both causal and anti-causal wavefield components, which suggests that the mean current is small. Picks converge to a constant phase speed around 0.2 Hz all along the cable segment, consistent with the deep water limit of the OSGW dispersion relation which is insensitive to water depth. At low frequencies (<0.15 Hz), the measured phase speed is approximately constant between 3 and 5 km distance, and then increases gradually over the last kilometer, indicating an increase in water depth. The modeled dispersion picks from Equation 8 (Figure 7b) reproduce these trends. The residual (Figure 7c) between measured and modeled dispersion is everywhere less than 10% of the measured phase speed, approaching zero at high frequencies. The modeled dispersion systematically under-predicts the highest phase speeds measured at low frequencies and over-predicts the phase speeds measured at intermediate frequencies, because the measured dispersion curves are more linear than the theoretical OSGW dispersion relation can produce for any set of parameters. In spite of the ∼1 m/s misfit at lower frequencies, the inverted depth profile (Figure 7d) accurately reproduces the bathymetric profile along the cable path interpolated from EMODnet Bathymetry Consortium (2020), with a maximum difference <5 m. The inverted profile captures the flat shelf up to 4.7 km, as well as the slope angle from 4.7 to 6 km, but is systematically too deep. This systematic difference may result from a mismatch in tidal datum between the measurements and the bathymetry model, poor interpolation of the bathymetry model in shallow water, or uncertainty in cable location, which is on the order of 100 m. The directional spectrum of ocean swell at low frequencies could also contribute to this difference, since waves arriving from an oblique azimuth appear with faster apparent phase speed along the cable direction. If the swell is highly anisotropic, such oblique incidence can yield a biased Green's function estimate, which could explain why the measured dispersion picks are under-predicted around 0.03–0.05 Hz (Figures 6c and 7c) and why the inverted profile is deeper (faster) than the bathymetry model (Figure 7d). Because the phase speed is highly sensitive to water depth at low frequencies $\left(\frac{\partial c}{\partial h} = \frac{g}{2}(gh)^{-1/2}\right)$, the 1σ uncertainty is always ≤ 1 m.

4.2. Tidal Current

The inverted mean current is within 1σ of 0 m/s across the entire cable segment (Figure 7d). This is expected since tidal currents dominate the flow in many shallow water settings. The M2 tide (12.4 hr) is the largest constituent, and divides about evenly into the 108-hr data set, so the mean flow should be negligible.

Combining the mean and differential current measurements results in a matrix of current velocity in space and time, shown in Figure 10a for all channel pairs with 300 m offset. The most prominent feature is sinusoidally time-dependent flow at the M2 tidal period, with an amplitude that begins around ±0.2 m/s on the first day of the experiment and gradually increases to +0.5/− 0.4 m/s on the last day. The current is locked in phase across the 3-km cable segment, and the only feature correlated to water depth is a small decrease in the current velocity from 5 to 6 km where the bathymetry is steeper and deeper. Over the first 3 days, the measured current is centered around zero mean, but starts to drift away from the reference toward positive values in the last 36 hr. This drift reflects the limitation of using a single reference state for differential current measurement over an extended time-lapse. Notably neither the high-frequency wave event nor the swell dispersion trend observed OSGW spectrograms in Figure 3 are evident in the final current results. The measured current time-series also include a pattern of jumps (up to 0.3 m/s difference in 1 hr) at the maximum positive current (flow toward the southwest along the cable), which is discussed in the following section.

Each pixel in Figure 10a represents the measurement from an independent pair of channels, so even considering the overlap of adjacent pairs, the map is remarkably smooth. In principle, a current velocity can be measured from all 45,150 NCFs and incorporated into a tomographic inversion to increase the spatial resolution and decrease uncertainties. In practice, this is a highly over-determined problem which requires strong regularization and considerable computational time for very little improvement. The difference between current measurements from 300-m (Figures 10a) and 600-m (Figure 10b) offset pairs is <0.05 m/s (Figures 10d and 10e), so the information is redundant. However, not all NCFs yield useful information. The path-integrated travel-time shifts (e.g., Figure 9) induced by currents were too small to measure reliably for channel pairs with offset <150 m. At offsets >1 km, attenuation of high frequency waves restricted the analysis to <0.1 Hz, resulting in high uncertainties.

Because no in-situ observations of current velocity are available, we compare our measured current velocity with a model of tidal flow generated by the OSU Tidal Prediction Software from the TPXO9 tidal solutions, which are a shallow-water model fit to global altimetry observations of sea-surface height (Egbert & Erofeeva, 2002). The TPXO9 prediction for the barotropic current is evaluated at each point along the 3-km cable segment for the dates of the experiment and projected onto the direction of the cable (Figure 10c). The measured current velocity accurately reproduces the principal properties of the model (Figure 10d). The amplitude matches both the long-term increasing trend over the 4.5-day time-lapse and the beating pattern of the M1 and M2 tides such that every

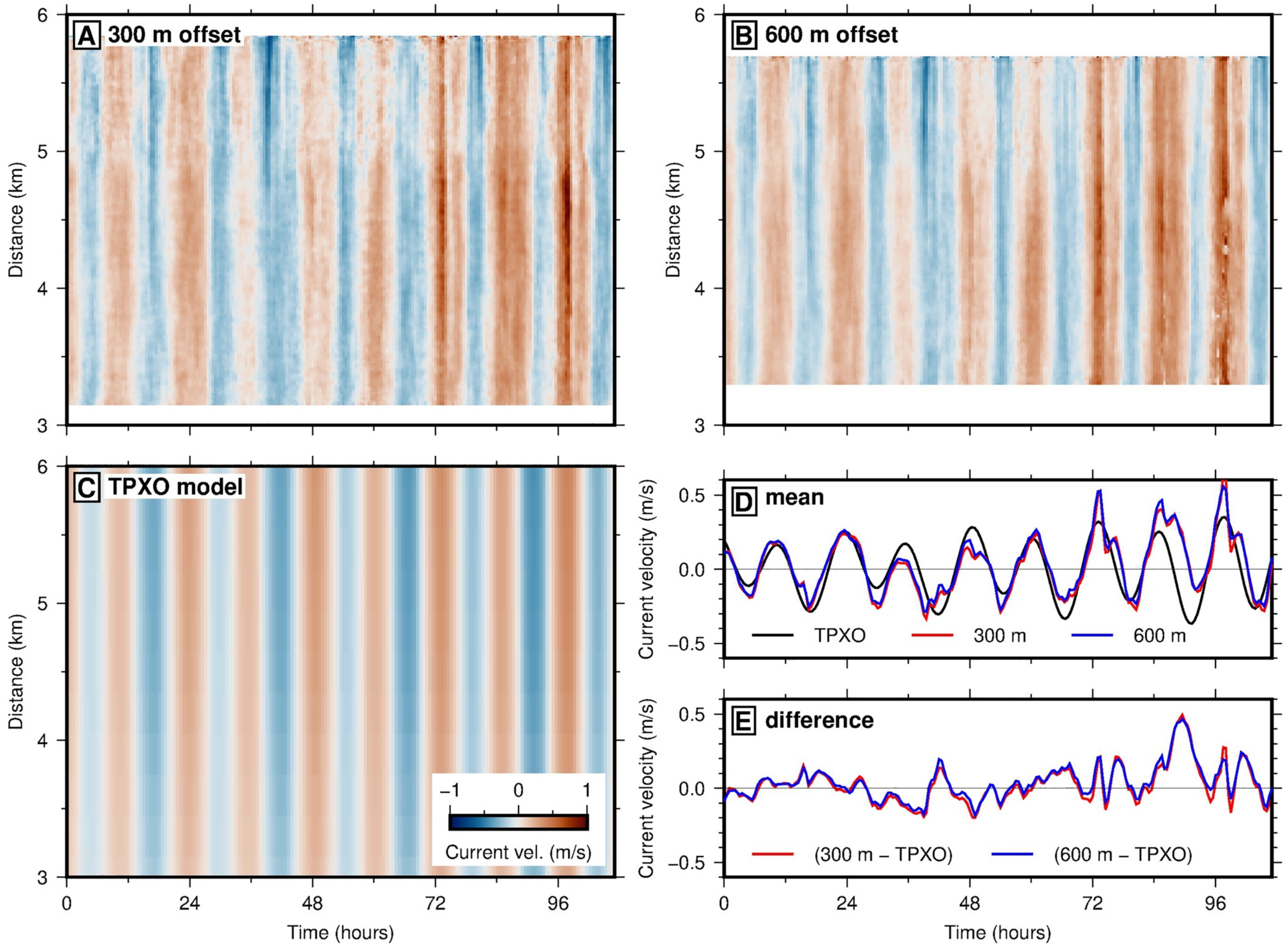

Figure 10. (a) Measured current velocity as a function of time and distance for all noise correlation function pairs with 300 m offset. (b) Same as (a) but for 600-m offset pairs. (c) Current velocity from the TPXO tidal model computed at each channel location for the time of the experiment and projected onto the azimuth of the cable. (d) Comparison of the mean TPXO-predicted tidal current velocity along the cable with the mean measured current velocity for all channel pairs with 300-m or 600-m offset. (e) Difference between results and TPXO model.

other 12-hr cycle has a smaller amplitude over the first three days. The TPXO9 model and measured current agree that the phase is constant along the 3-km cable segment. The sharp jumps during the last 36 hr cannot be accounted for by ordinary tidal harmonic constituents.

5. Discussion

While the results of ocean current measurement by interferometry of the ambient OSGW field compare favorably to the TPXO9 solution for the barotropic tide, several outstanding features deserve further discussion. Significantly, the last 36 hr exhibit several sharp jumps in current velocity at non-tidal frequencies and a systematic discrepancy in phase relative to the tidal model. In order to verify that the observed jumps in current velocity are features of the raw data and not artifacts of our particular processing methodology, we first compare our results with FK spectra following the simple approach of Williams et al. (2019). The complete 3-km cable segment is divided into hourly windows, two Fourier transforms are applied to obtain the FK spectrum for each time window, the FK spectrum is transformed into coordinates of phase speed versus frequency using the coordinate transform $c = f/k$, and the mean current velocity measured along the cable is super-imposed. Six consecutive hours are plotted in Figure 11 as an example, zoomed in to a small part of the spectrum where the dispersion relation is approximately linear. In these coordinates, the OSGW energy is concentrated in a packet that sits

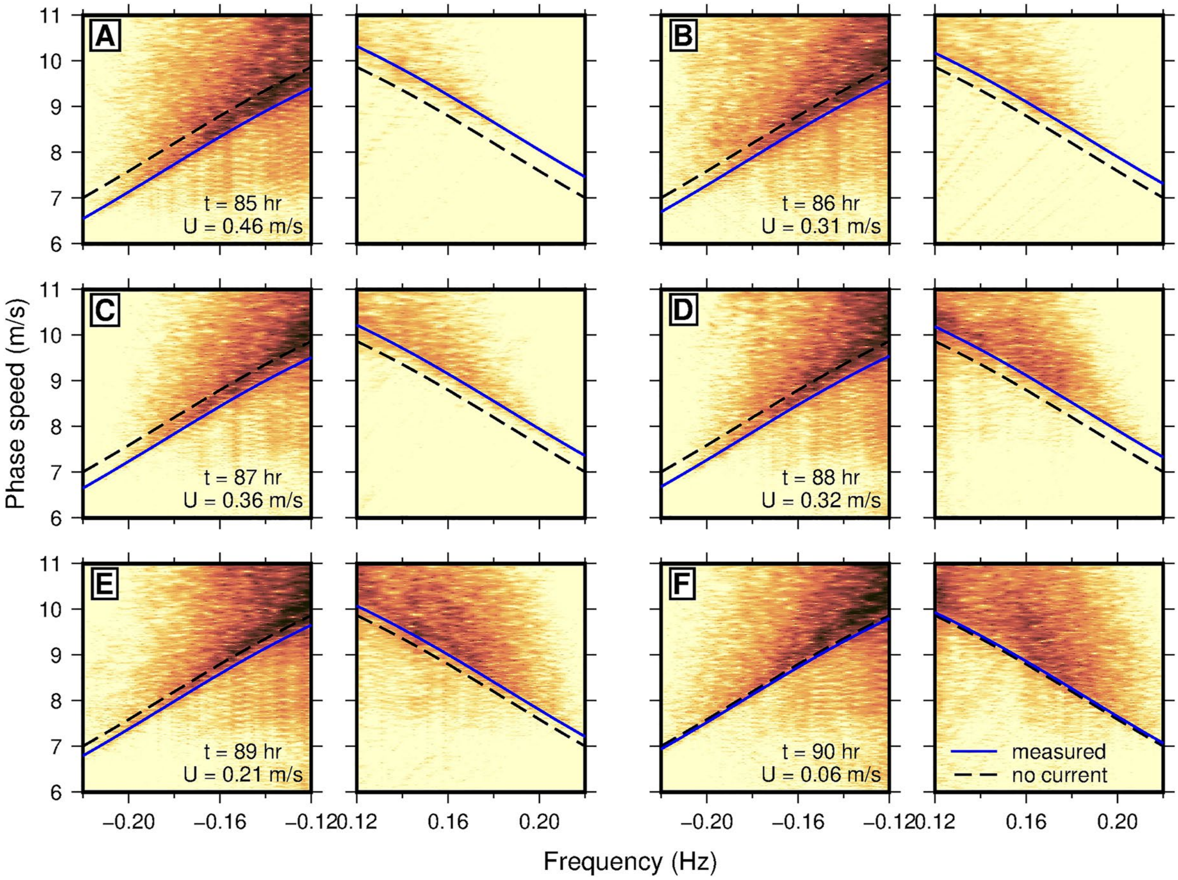

Figure 11. Comparison of current velocities measured with ocean surface gravity wave (OSGW) interferometry and the modified stretching method to hourly frequency-wavenumber (FK) spectra computed from the raw data. Each FK spectrum has been transformed to coordinates of phase speed versus frequency and only a small area of the spectrum is shown. Panels (a–f) are computed for consecutive hours, with the landward-propagating (anti-causal) component on the left and the seaward-propagating (causal) component on the right. The same theoretical dispersion relation for OSGW in the absence of a current (Equation 1) is plotted on all panels in black, and the measured wave-current dispersion relation for each time window is plotted in blue.

above the dispersion relation for a wave propagating along the cable direction, so the lower-velocity edge, which is quite sharp, is the target of visual comparison. As expected, the FK spectra exhibit a non-reciprocal shift in the dispersion relation (Doppler shift) that evolves over time, and generally corresponds to the OSGW interferometry solution, including the sharp jumps in current velocity during the last 36 hr. These jumps are thus present in the raw data and likely a signature of real flow patterns.

One possible origin for the sharp variations in measured current velocity is by interaction of surface and internal gravity waves. Internal solitary waves generated every 12–24 hr by tidal flow over the Camarinal Sill (Figure 1) have been observed frequently by satellites and moorings, propagating east through the Strait of Gibraltar across the cable path (Ziegenbein, 1970). Their typical propagation speed is 0.5–2 m/s, with a wavelength (inter-soliton distance) of 0.5–2 km and a period of 10–15 min, though these parameters vary considerably among observations and their shallow-water shoaling behavior on the shelf has not been studied (Brandt et al., 1996; Watson & Robinson, 1990; Ziegenbein, 1970). Because the wavelength is much longer and the speed is much slower than OSGWs, the interaction of internal waves with short surface waves is comparable to advection by a surface current (Alpers, 1985; Lenain & Pizzo, 2021). The propagation time of an internal wave from the Camarinal Sill to the 3–6 km cable segment is about 2–4 hr at these speeds, so the timing of the sharp jumps in our current velocity time-series is consistent with this interpretation, as is the sole occurrence of these features immediately following the maximum southwestward (Mediterranean outflow) current (Vázquez et al., 2008). Because the finest temporal resolution of the current measurements is 0.5 hr, such an internal solitary wave would appear as a near-instantaneous jump in flow velocity along the cable segment, which is also consistent with our measurements. However, the pattern of the jumps (gradual increase in flow to the southwest followed by a sharp decrease) is opposite to the polarity that would be predicted for an internal wave of depression (Alpers, 1985; Lamb, 1997). Internal wave interaction is also predicted to modulate the directional spectrum and height of surface waves, and while we noted evidence of wave-current interaction at tidal periods, no sharp modulations in wave spectra are apparent at the time of the jumps in current velocity during the last 36 hr (Figure 3).

5.1. Sources of Bias

We proposed that these features could relate to internal solitary waves, which have been observed in the Strait of Gibraltar, but, with no complementary data to support a physical interpretation and considering the generalizability of this method to other ocean environments, it is necessary to constrain sources of observational bias as well as the sensitivity of OSGW interferometry. One major source of potential bias in ambient noise interferometry is the heterogeneous distribution of sources in real earth environments. This problem has been recognized in seismology, but is largely ignored despite potentially introducing significant errors into tomographic velocity models (Yao & Van Der Hilst, 2009). The anisotropic nature of the ocean wave directional spectrum makes this a particular challenge for OSGW interferometry. The ambient OSGW field is frequently modeled using a point spectrum $S(\omega)$ and a directional spreading function $D(\omega, \theta)$, such that the wave directional spectrum is a function of both azimuth and frequency ($S(\omega, \theta) = S(\omega)D(\omega, \theta)$; Ochi, 1998). Commonly, the spreading term D is expressed as a power of $\cos(\theta)$, resulting in a very narrow directional spectrum. In the limiting case of a single stationary source, cross-correlation of the wave records at two points yields a distorted representation of the Green's function according to the azimuth of the source ($k' = k/\cos(\theta)$). For a diffuse and isotropic source distribution, the same cross-correlation yields an exact representation of the Green's function, as in Equation 6. For realistic OSGW source distributions, the scenario is likely somewhere between the two. As discussed previously, the overestimated OSGW phase speed at low frequencies in Figure 7c and the misfit between observed and predicted bathymetry in Figure 7d are possibly a result of bias from an anisotropic OSGW directional spectrum. Because the OSGW energy around 0.1 Hz is dominated by swell from a distant source, the low-frequency component of the wave spectrum is likely to be more anisotropic. Because the apparent speed of a wave measured between two stations can only increase with obliquity and OSGW phase speed increases with water depth, if the dominant direction of OSGW propagating across the array is at an angle to the cable direction, OSGW interferometry will yield a water depth too deep. This effect can be corrected if the dominant wave azimuth is known.

We follow after Lu (2015) in constructing synthetic datasets to test the effect of anisotropic, time-dependent source distributions. A 12-hr synthetic recording of random waves is generated by convolving a Ricker wavelet with the OSGW Green's function for seafloor pressure at 120,000 randomly distributed source locations and two receivers. Then, cross-correlation and stretching are applied to the synthetic data set to extract the apparent time-lapse of current velocity. This is illustrated in Figure 12a where the random wavefield from a spatially uniform distribution of far-field sources is recorded in the presence of a current with a period of 12 hr and amplitude of 0.5 m/s oriented at 45° to the cable direction. The result (Figure 12b) is that the component of flow along the direction of the cable is successfully recovered, as predicted by theory. Next, we consider no current but an azimuthally bimodal normal distribution of sources, which rotates by 20° in the same direction as a function of time (Figure 12c). Stretching only the causal or anti-causal side of the cross-correlation results in a spurious apparent current (Figure 12d); however, incorporating both components into the DACC, these terms cancel out so that the observed current (none) is correct. If instead the two peaks of the source distribution rotate symmetrically in opposite directions over time (Figure 12e), the resulting spurious current measurements add together to simulate a tidal current (Figure 13). Yet, the spurious current is small—a rotation of 20° for both source clusters results in a 0.2 m/s current. These scenarios mimic, for example, a coastal OBDAS array where wind waves reflect from shallow water to generate a bimodal directional spectrum. Therefore, in many but not all cases, the incorporation of non-reciprocal paths directly into the stretching workflow mitigates the bias introduced by an anisotropic and time-dependent distribution of sources.

The strong local modulation of waves by tides, as observed in Figure 3, must also be excluded as a source of bias. In particular, conventional time-domain application of the stretching method in coda wave interferometry is known to introduce spurious velocity changes due to variations in the source amplitude spectrum (Zhan et al., 2013). We chose to apply stretching in the frequency domain in order to mitigate this effect. We repeated our synthetic

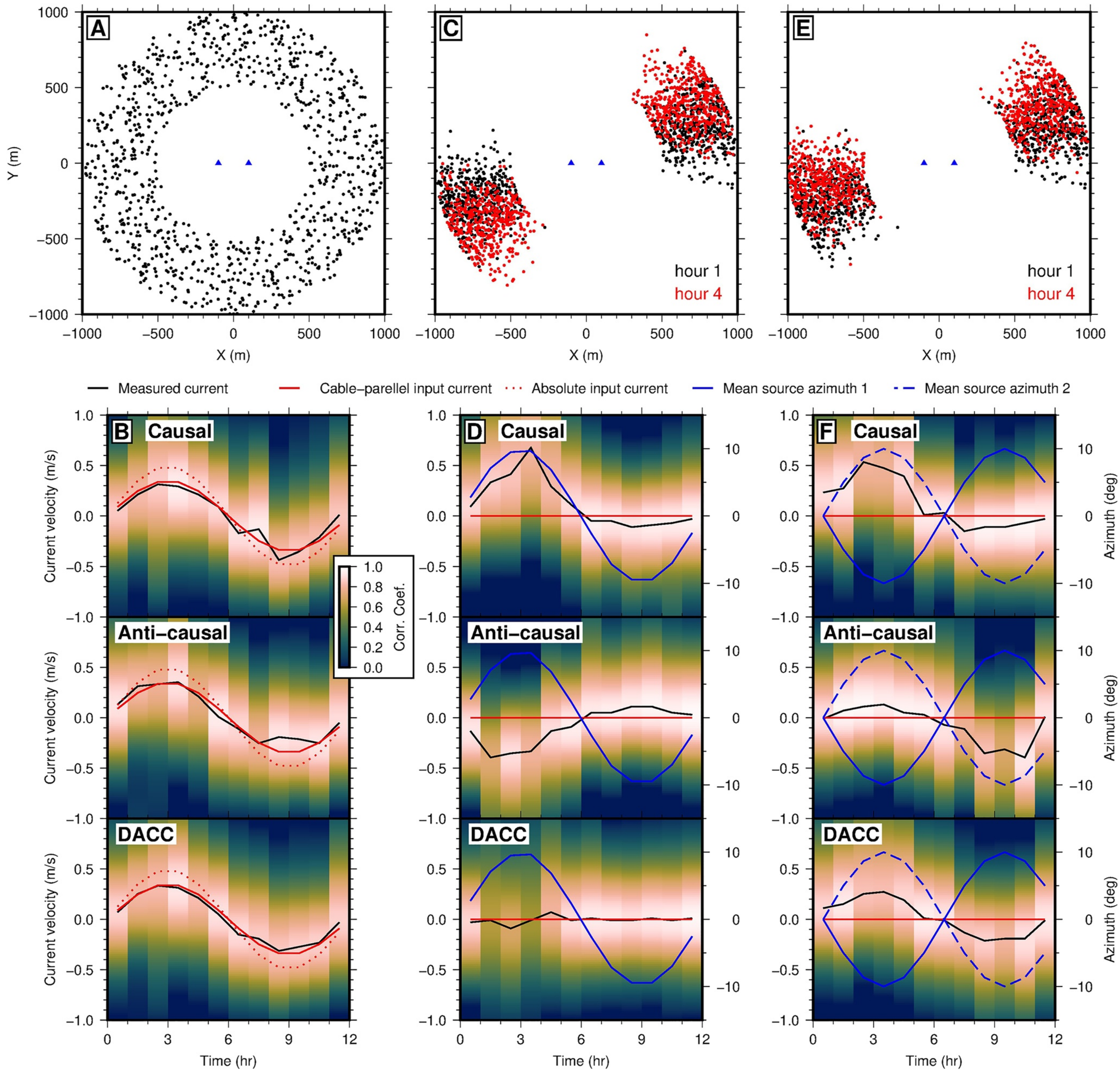

Figure 12. Synthetic ocean surface gravity wave (OSGW) interferometry and stretching. (a) A uniform, far-field OSGW source distribution (black dots) recorded at two channels (black triangles) in the presence of a current oriented at 45° from the *x*-axis. (b) Results of cross-correlating and stretching the synthetic data from (a), showing that the component of the current along the *x*-axis is recovered, not the absolute current. (c) A bimodal OSGW source distribution that rotates symmetrically by 20° at 12-hr period. (d) Results of the synthetic data from (c) showing that Doppler-averaging cancels out spurious current measurements. (e) A bimodal OSGW source distribution that rotates asymmetrically by 20° over 12-hr period. (f) Results of the synthetic data from (e) showing that a small spurious current is measured in this unique case.

analysis with the same uniform source distribution as Figure 12a above but varied the center frequency of the source wavelet between 0.15 ± 0.02 Hz continuously at 12-hr period (which is comparable to the observation in Figure 3c). The result (Figure 13a) shows that changing the amplitude spectrum does not introduce a spurious current here. Similarly, the effect of tides on water column depth modulates OSGW dispersion. We also repeated our synthetic analysis varying the water depth between 15 ± 1 m at 12-hr period (Figure 13b). The changing water depth can introduce a small spurious current in the stretching results for each individual directional component; however, the effect is reciprocal and eliminated by Doppler-averaging. The spurious current measured for each

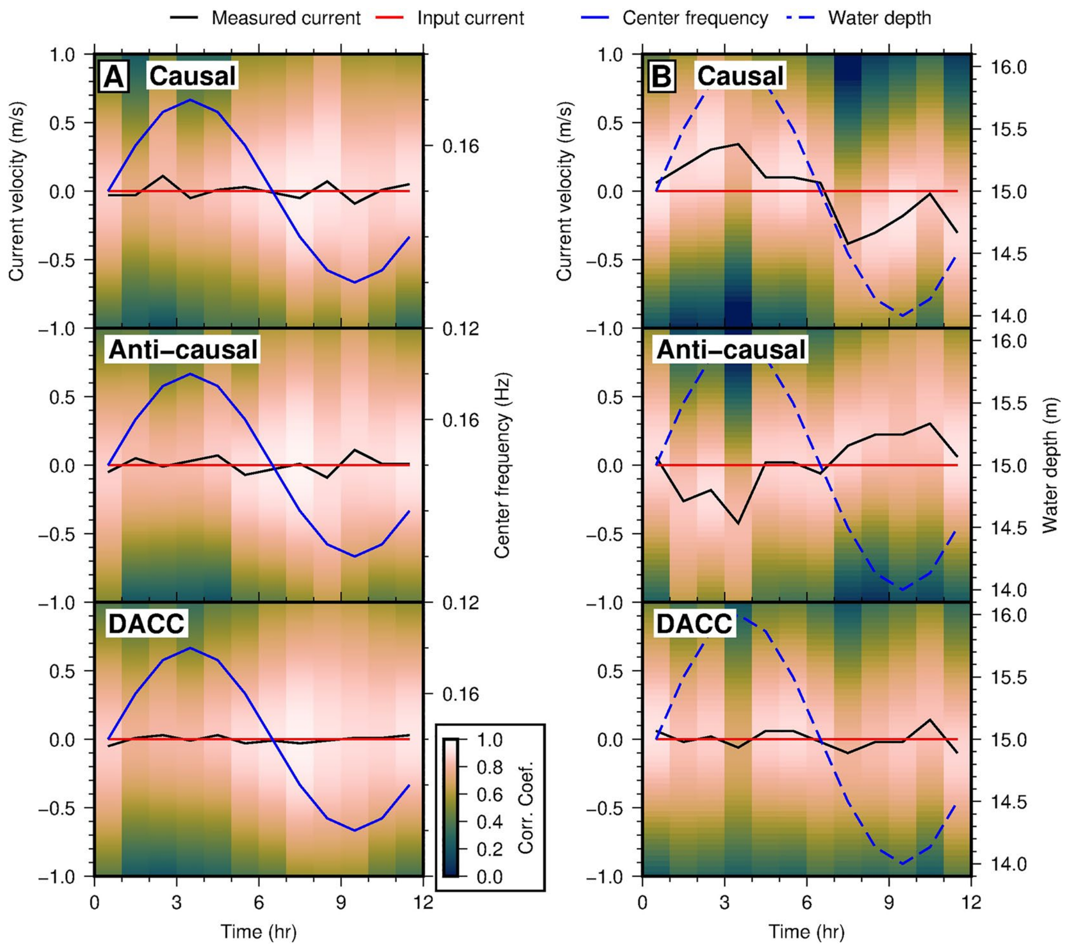

Figure 13. Synthetic ocean surface gravity wave interferometry and stretching results with the same source distribution as Figure 12a. (a) The center frequency of the source wavelet varies at 12-hr period, and no spurious current is measured but the correlation coefficient is lower. (b) The water depth varies at 12-hr period, resulting in a spurious current that cancels out through Doppler-averaging.

directional component is also in-phase with the sea surface height, which is typically 90° out of phase with the flow for tidal currents. Note that for both Figures 13a and 13b the maximum correlation coefficient is much lower and the width of the correlation coefficient peak (which is implicitly tied to uncertainty) is much broader than in Figure 12. This is because changing the frequency content or dispersion relation results in low waveform coherence. Other conditions not considered here that could contribute to a non-reciprocal bias include measurement bias from recording the horizontal component of strain or pressure on a sloping bottom, non-linear energy transfer between waves and the current or breaking of waves, and retardation of waves by shoaling (e.g., the mild-slope equation). Overall, no single source of bias is evident that easily describes the sharp deviations from the TPXO tidal current model in Figure 10, suggesting these are physical signals of complex flow.

5.2. Depth Sensitivity

In this study we have so far only considered the simple case of OSGW propagating in a uniform current (Equation 9), but depth-dependent flow is common, especially in coastal environments. Not only is the assumption of uniform flow then a potential source of bias, but constraining the vertical structure of currents can be significant for understanding processes like sediment transport and mixing. Consider, for example, the case of a linear shear current: $\frac{\partial U}{\partial z} = U_s s'$, where U_s is the surface current and $s' \in [0, h^{-1}]$ a constant such that $s' = h^{-1}$ represents no flow at the bottom. Linearization of the relevant dispersion relation (Kirby & Chen, 1989) yields

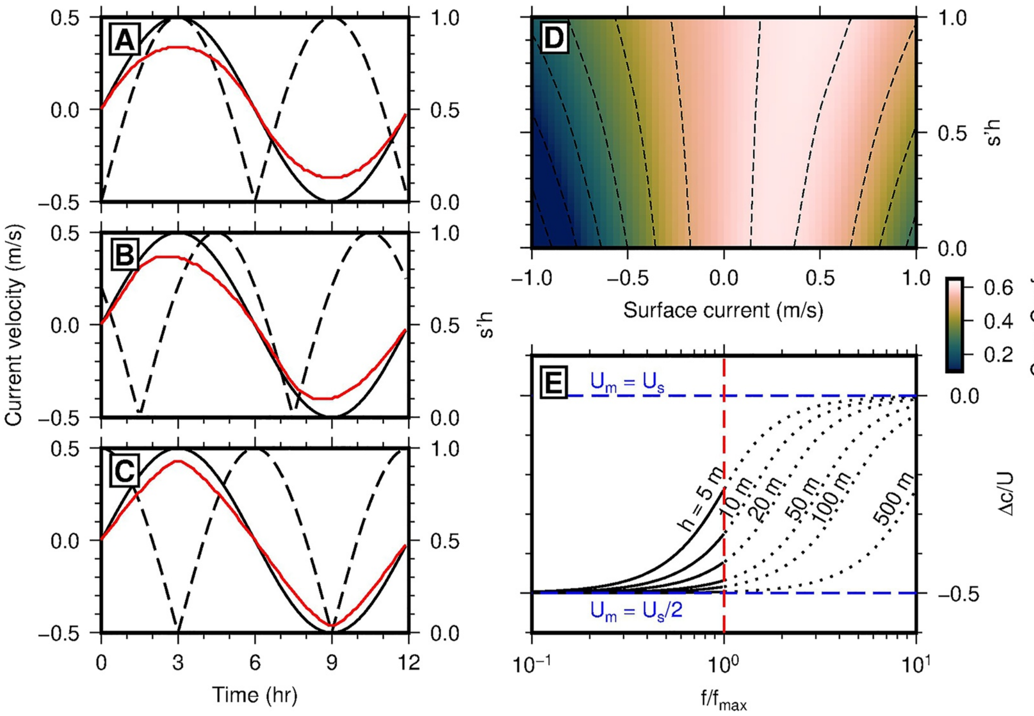

Figure 14. (a–c) Synthetic example demonstrating how a shear current can bias the results of the modified stretching method if a uniform current model is used. The input velocity gradient ($s' = (1/U)\partial U/\partial z$, black dashed line) is advanced in phase by (a) 0, (b) 45, and (c) 90° relative to the input surface current (black solid line) in each panel. The measured current (red line), can become rounded, sharpened, or asymmetrical. (d) Example doppler-averaged correlation coefficient matrix from stretching an example noise cross-correlation functions using the dispersion relation for a linear shear current and searching over two parameters (U, s'). (e) Difference in current velocity between a linear shear current and a uniform current for different water depths. The solid black lines represent the range that can be observed from ocean-bottom pressure measurements ($f < f_{\max}$).

$$c\left(\omega, U_0, s'\right) = c_0(\omega) + \left(1 - \frac{s' c_0(\omega)^2}{2g}\right) U_s. \tag{12}$$

Generating synthetic data for OSGW propagating in a shear current as above and inverting for the uniform current speed using the incorrect dispersion relation (Equation 9), Figures 14a–14c demonstrates how the shape and amplitude of the current measurement can be biased. In particular, if the vertical structure s' is out of phase with the tidal surface current U_s, such as may result from bottom friction, the apparent phase of the measured current can change significantly (Figure 14b).

Parameterizing differential current measurement by stretching with Equation 12 and solving for an additional parameter, however, is challenging because s' and U_s co-vary. We re-calculated the stretching results for the Strait of Gibraltar DAS array with a shear model but were unable to recover a coherent map of s'. This is illustrated in Figure 14d, which shows an example grid-search of the DACC for a single NCF pair for the two-parameter case in Equation 12. Whether measuring depth-varying flow is possible depends on the bandwidth over which NCFs are obtained, which is modulated by water depth (Figure 14e). For the limiting case where $s' = h^{-1}$, the mean current is simply $U_m = U_s/2$. Therefore, at low frequencies (in the shallow water limit), $\Delta c = \left(1 - \frac{c_0^2}{2gh}\right) U_s - U_m \approx \frac{1}{2} U_s - U_m = 0$, so the correct depth-averaged current velocity can be recovered but no depth-dependent information can be discerned. Similarly, at high frequencies (in the deep water limit) $\Delta c \approx U_s - U_m = \frac{1}{2} U_s$, so OSGW are only sensitive to the surface flow, resulting in both an overestimated current velocity (by a factor of two) and no depth-dependent information. Such deep-water waves, however, cannot be observed at the bottom. Constraining vertical structure thereby requires observation of intermediate frequencies. Recalling the observational constraint that $f < f_{\max}$ (Equation 3), Figure 14e demonstrates that intermediate frequencies can only be recorded by OBDAS in very shallow water ($h \lesssim 10$ m), which further helps explain why the sensitivity is so low here (Figure 14d). OSGW interferometry with OBDAS may therefore be well suited for vertically sheared flows in rivers or estuaries, whereas surface measurements (such as attempted by Brown and Lu, 2016) may be needed to constrain depth-dependent structure in oceanic settings.

6. Conclusions

We have demonstrated that ocean current velocity can be measured along pre-existing submarine fiber-optic cables using DAS and ambient noise interferometry. Raw OBDAS records from the Strait of Gibraltar contain OSGW signals between 0.03–0.3 Hz, including both wind waves and swell. Applying a directional (FK) filter, we split the OSGW field into two directional components and calculated cross-correlations for each, resulting in an empirical approximation of the OSGW Green's function for reciprocal paths between each pair of channels along the OBDAS array. Then, introducing a two-step workflow, we measured the OSGW dispersion relation along the cable and extracted a 1D profile of water depth and 2D matrix (distance vs. time) of current velocity. Our results correlate well with a tidal current model, though some sharp, anomalous changes in current velocity over the last 36 hr of the data set may relate to internal waves. Numerical experiments demonstrate that by exploiting reciprocal measurements we mitigate potential bias from a non-uniform source distribution and time-varying wave spectrum in most but not all cases. Such capabilities for bathymetric profiling and flow monitoring indicate the broad scope of applications for OBDAS in observational physical oceanography.

Conflict of Interest

The authors declare no conflicts of interest relevant to this study.

Data Availability Statement

The data used in this paper are proprietary and not available for public release. However, the code necessary to reproduce the methods of this paper is available at https://github.com/ethanfwilliams/OSGW_interferometry_tutorial, using the public data set of Williams et al. (2019) (http://dx.doi.org/10.22002/D1.1296).

Acknowledgments

We thank Red Eléctrica de España for access to their cable and Aragon Photonics for providing the interrogator unit. E. F. Williams was supported by an NSF Graduate Research Fellowship. Z. Zhan acknowledges support from the Moore Foundation and NSF under CAREER Award 1848166. M. R. Fernández-Ruiz acknowledges support from the Spanish MICINN under contract IJC2018-035684-I. M. González-Herráez acknowledges support from projects RTI2018-097957-B-C31 and RTI2018-097957-B-C33 funded by the Spanish Ministry of Science and Innovation, project SINFOTON2-CM: P2018/NMT-4326 funded by Comunidad de Madrid and Fondo Europeo de Desarrollo Regional (FEDER) Program, and project PLEC2021-007875 funded by the Spanish Ministry of Science and Innovation MCIN/AEI/10.13039/501100011033 and by the European Union NextGenerationEU/PRTR program.

References

Alpers, W. (1985). Theory of radar imaging of internal waves. *Nature*, *314*(21), 245–247. https://doi.org/10.1038/314245a0

Bensen, G. D., Ritzwoller, M. H., Barmin, M. P., Levshin, A. L., Lin, F., Moschetti, M. P., et al. (2007). Processing seismic ambient noise data to obtain reliable broad-band surface wave dispersion measurements. *Geophysical Journal International*, *169*(3), 1239–1260. https://doi.org/10.1111/j.1365-246x.2007.03374.x

Brandt, P., Alpers, W., & Backhaus, J. O. (1996). Study of the generation and propagation of internal waves in the strait of Gibraltar using a numerical model and synthetic aperture radar images of the European ERS1 satellite. *Journal of Geophysical Research*, *101*(C6), 14237–14252. https://doi.org/10.1029/96jc00540

Brown, M. G., Godin, O. A., Williams, N. J., Zabotin, N. A., Zabotina, L., & Banker, G. J. (2014). Acoustic Green's function extraction from ambient noise in a coastal ocean environment. *Geophysical Research Letters*, *41*(15), 5555–5562. https://doi.org/10.1002/2014gl060926

Brown, M. G., & Lu, C. (2016). Green's function retrieval in a field of random water waves. *Wave Motion*, *60*, 8–19. https://doi.org/10.1016/j.wavemoti.2015.08.003

Campillo, M., & Paul, A. (2003). Long-range correlations in the diffuse seismic coda. *Science*, *299*(5606), 547–549. https://doi.org/10.1126/science.1078551

Crawford, W. C. (2004). The sensitivity of seafloor compliance measurements to sub-basalt sediments. *Geophysical Journal International*, *157*(3), 1130–1145. https://doi.org/10.1111/j.1365-246x.2004.02264.x

Crawford, W. C., Webb, S. C., & Hildebrand, J. A. (1991). Seafloor compliance observed by long-period pressure and displacement measurements. *Journal of Geophysical Research*, *96*(B10), 16151–16160. https://doi.org/10.1029/91jb01577

Doran, A. K., & Laske, G. (2016). Infragravity waves and horizontal seafloor compliance. *Journal of Geophysical Research: Solid Earth*, *121*(1), 260–278. https://doi.org/10.1002/2015jb012511

Dushaw, B. D., Worchester, P. F., Cornuelle, B. D., & Howe, B. M. (1994). Barotropic currents and vorticity in the central north Pacific in summer 1987 determined from long-range acoustic transmissions. *Journal of Geophysical Research*, *99*, 3262–3272.

Egbert, G. D., & Erofeeva, S. Y. (2002). Efficient inverse modeling of barotropic ocean tides. *Journal of Atmospheric and Oceanic Technology*, *19*(2), 183–204. https://doi.org/10.1175/1520-0426(2002)019<0183:eimobo>2.0.co;2

Elgar, S., & Guza, R. (1985). Observations of bispectra of shoaling surface gravity waves. *Journal of Fluid Mechanics*, *161*(-1), 425–448. https://doi.org/10.1017/s0022112085003007

EMODnet Bathymetry Consortium. (2020). *Emodnet digital bathymetry (dtm)*.

Fernandez-Ruiz, M. R., Costa, L., & Martins, H. F. (2019). Distributed acoustic sensing using chirped-pulse phase-sensitive OTDR technology. *Sensors*, *19*(20), 4368. https://doi.org/10.3390/s19204368

Fernandez-Ruiz, M. R., Martins, H. F., Costa, L., Martin-Lopez, S., & Gonzalez-Herraez, M. (2018). Steady-sensitivity distributed acoustic sensors. *Journal of Lightwave Technology*, *36*(23), 5690–5696. https://doi.org/10.1109/jlt.2018.2877849

Godin, O. A. (2006). Recovering the acoustic green's function from ambient noise cross correlation in an inhomogeneous moving medium. *Physical Review Letters*, *97*(5), 054301. https://doi.org/10.1103/physrevlett.97.054301

Godin, O. A. (2018). Acoustic noise interferometry in a time-dependent coastal ocean. *Journal of the Acoustical Society of America*, *143*(2), 595–604. https://doi.org/10.1121/1.5022287

Godin, O. A., Brown, M. G., Zabotin, N. A., Zabotina, L. Y., & Williams, N. J. (2014). Passive acoustic measurement of flow velocity in the Straits of Florida. *Geoscience Letters*, *1*, 16. https://doi.org/10.1186/s40562-014-0016-6

Godin, O. A., Zabotin, N. A., & Goncharov, V. V. (2010). Ocean tomography with acoustic daylight. *Geophysical Research Letters*, *37*(13), L13605. https://doi.org/10.1029/2010gl043623

Godin, O. A., Zabotin, N. A., Sheehan, A. F., & Collins, J. A. (2014). Interferometry of infragravity waves off New Zealand. *Journal of Geophysical Research: Oceans*, *119*(2), 1103–1122. https://doi.org/10.1002/2013jc009395

Harmon, N., Henstock, T., Srokosz, M., Tilmann, F., Rietbrock, A., & Barton, P. (2012). Infragravity wave source regions determined from ambient noise correlation. *Geophysical Research Letters*, *39*(4), L04604. https://doi.org/10.1029/2011gl050414

Herbers, T. H. C., Elgar, S., & Guza, R. T. (1995). Generation and propagation of infragravity waves. *Journal of Geophysical Research*, *100*(C12), 24863–24872. https://doi.org/10.1029/95jc02680

Herbers, T. H. C., Orzech, M., Elgar, S., & Guza, R. (2003). Shoaling transformation of wave frequency-directional spectra. *Journal of Geophysical Research*, *108*(C1), 3013. https://doi.org/10.1029/2001jc001304

Howe, B. M., Worchester, P. F., & Spindel, R. C. (1987). Ocean acoustic tomography: Mesoscale velocity. *Journal of Geophysical Research*, *92*(C4), 3785–3805. https://doi.org/10.1029/jc092ic04p03785

Ide, S., Araki, E., & Matsumoto, H. (2021). Very broadband strain-rate measurements along a submarine fiber-optic cable off Cape Muroto, Nankai subduction zone, Japan. *Earth Planets and Space*, *73*, 63. https://doi.org/10.1186/s40623-021-01385-5

Kirby, J. T., & Chen, T.-M. (1989). Surface waves on vertically sheared flows: Approximate dispersion relations. *Journal of Geophysical Research*, *94*(C1), 1013–1027. https://doi.org/10.1029/jc094ic01p01013

Lamb, K. G. (1997). Particle transport by non-breaking, solitary internal waves. *Journal of Geophysical Research*, *102*(C8), 18641–18660. https://doi.org/10.1029/97jc00441

Latychev, K., & Edwards, R. (2003). On the compliance method and the assessment of three-dimensional seafloor gas hydrate deposits. *Geophysical Journal International*, *155*(3), 9223–9952. https://doi.org/10.1111/j.1365-246x.2003.02090.x

Lenain, L., & Pizzo, N. (2021). Modulation of surface gravity waves by internal waves. *Journal of Physical Oceanography*, *51*, 2735–2748. https://doi.org/10.1175/jpo-d-20-0302.1

Lin, J., Kaneko, A., Godha, N., & Yamaguchi, K. (2005). Accurate imaging and prediction of Kanmon Strait tidal current structures by the coastal acoustic tomography data. *Geophysical Research Letters*, *32*(14), L14607. https://doi.org/10.1029/2005gl022914

Lindsey, N. J., Dawe, T. C., & Ajo-Franklin, J. B. (2019). Illuminating seafloor faults and ocean dynamics with dark fiber distributed acoustic sensing. *Science*, *366*(6469), 1103–1107. https://doi.org/10.1126/science.aay5881

Lindsey, N. J., & Martin, E. R. (2021). Fiber-optic seismology. *Annual Review of Earth and Planetary Sciences*, *49*(1), 309–336. https://doi.org/10.1146/annurev-earth-072420-065213

Lindsey, N. J., Rademacher, H., & Ajo-Franklin, J. B. (2020). On the broadband instrument response of fiber-optic DAS arrays. *Journal of Geophysical Research: Solid Earth*, *125*(2), e2019JB018145. https://doi.org/10.1029/2019jb018145

Lior, I., Sladen, A., Rivet, D., Ampuero, J.-P., Hello, Y., Becerril, C., et al. (2021). On the detection capabilities of underwater distributed acoustic sensing. *Journal of Geophysical Research: Solid Earth*, *126*(3), e2020JB020925. https://doi.org/10.1029/2020jb020925

Lobkis, O. I., & Weaver, R. L. (2001). On the emergence of the Green's function in the correlations of a diffuse field. *Journal of the Acoustical Society of America*, *110*(6), 3011–3017. https://doi.org/10.1121/1.1417528

Longuet-Higgins, M. S. (1950). A theory of the origin of microseisms. *Phylosophical Transactions of the Royal Society A*, *243*(857), 1–35.

Lu, C. (2015). *Water wave Green's function retrieval from a random wave field*. (Unpublished doctoral dissertation). University of Miami.

Martin, E. R., Lindsey, N. J., Ajo-Franklin, J. B., & Biondi, B. (2018). Introduction to interferometry of fiber optic strain measurements. *EarthArXiv*, 1–33.

Matsumotu, H., Araki, E., Kimura, T., Fujie, G., Shiraishi, K., Tonegawa, T., et al. (2021). Detection of hydroacoustic signals on a fiber-optic submarine cable. *Scientific Reports*, *11*, 2797. https://doi.org/10.1038/s41598-021-82093-8

Mecozzi, A., Cantono, M., Castellanos, J. C., Kamalov, V., Muller, R., & Zhan, Z. (2021). Polarization sensing using submarine optical cables. *Optica*, *8*(6), 788–795. https://doi.org/10.1364/optica.424307

Neale, J., Harmon, N., & Srokosz, M. (2015). Source regions and reflection of infragravity waves offshore the U.S. Pacific Northwest. *Journal of Geophysical Research: Oceans*, *120*(9), 6474–6491. https://doi.org/10.1002/2015jc010891

Ochi, M. K. (1998). *Ocean waves: The stochastic approach*.

Paitz, P., Edme, P., Graff, D., Walter, F., Doetsch, J., Chalari, A., et al. (2021). Empirical investigations of the instrument response of distributed acoustic sensing (DAS) across 17 octaves. *Bulletin of the Seismological Society of America*, *111*(1), 1–10. https://doi.org/10.1785/0120200185

Pastor-Graells, J., Martins, H., Garcia-Ruiz, A., Martin-Lopez, S., & Gonzalez-Herraez, M. (2016). Single-shot distributed temperature and strain tracking using direct detection phase-sensitive OTDR with chirped pulse. *Optics Express*, *24*(12), 13121–13133. https://doi.org/10.1364/oe.24.013121

Pierson, W. J., & Moskowitz, L. (1964). A proposed spectral form for fully developed wind seas based on the similarity theory of S. A. Kitaigorodskii. *Journal of Geophysical Research*, *69*(24), 5181–5190. https://doi.org/10.1029/jz069i024p05181

Roux, P. A., & Kuperman, W. A., & the NPAL Group. (2004). Extracting coherent wave fronts from acoustic ambient noise in the ocean. *Journal of the Acoustical Society of America*, *116*(4), 1995–2003. https://doi.org/10.1121/1.1797754

Sens-Schönfelder, C., & Wegler, U. (2006). Passive image interferometry and seasonal variations of seismic velocities at Merapi volcano (Indonesia). *Geophysical Research Letters*, *33*(21), L21302. https://doi.org/10.1029/2006gl027797

Shapiro, N. M., Campillo, M., Stehly, L., & Ritzwoller, M. H. (2005). High-resolution surface-wave tomography from ambient seismic noise. *Science*, *307*(5715), 1615–1618. https://doi.org/10.1126/science.1108339

Sladen, A., Rivet, D., Ampuero, J.-P., de Barros, L., Hello, Y., Calbris, G., & Lamare, P. (2019). Distributed sensing of earthquakes and ocean-solid earth interactions on seafloor telecom cables. *Nature Communications*, *10*(1), 1–8. https://doi.org/10.1038/s41467-019-13793-z

Tonegawa, T., Fukao, Y., Shiobara, H., Ito, A., & Yamashita, M. (2018). Excitation location and seasonal variation of transoceanic infragravity waves observed at an absolute pressure gauge array. *Journal of Geophysical Research: Oceans*, *120*(1), 40–52. https://doi.org/10.1002/2017jc013488

Vázquez, A., Bruno, M., Izquierdo, A., Macías, D., & Ruiz-Cañavate, A. (2008). Meteorologically forced subinertial flows and internal wave generation at the main sill of the Strait of Gibraltar. *Deep-Sea Research I*, *55*(10), 1277–1283. https://doi.org/10.1016/j.dsr.2008.05.008

Watson, G., & Robinson, I. S. (1990). A study of internal wave propagation in the strait of Gibraltar using shore-based marine radar images. *Journal of Physical Oceanography*, *20*, 374–395.

Webb, S. C. (1986). Coherent pressure fluctuations observed at two sites on the deep sea floor. *Geophysical Research Letters*, *13*(2), 141–144. https://doi.org/10.1029/gl013i002p00141

Webb, S. C. (1998). Broadband seismology and noise under the ocean. *Reviews of Geophysics*, *36*(1), 105–142. https://doi.org/10.1029/97rg02287

Webb, S. C., Zhang, X., & Crawford, W. (1991). Infragravity waves in the deep ocean. *Journal of Geophysical Research*, *96*(C2), 2723–2736. https://doi.org/10.1029/90jc02212

Williams, E. F., Fernandez-Ruiz, M. R., Magalhaes, R., Vanthillo, R., Zhan, Z., Gonzalez-Herraez, M., & Martins, H. F. (2019). Distributed sensing of microseisms and teleseisms with submarine dark fibers. *Nature Communications*, *10*(5778), 1–16. https://doi.org/10.1038/s41467-019-13262-7

Worchester, P. F. (1977). Reciprocal acoustic transmission in a midocean environment. *Journal of the Acoustical Society of America*, *62*(4), 895–905. https://doi.org/10.1121/1.381619

Yamamoto, T., & Torii, T. (1986). Seabed shear modulus profile inversion using surface gravity (water) wave-induced bottom motion. *Geophysical Journal of the Royal Astronomical Society*, *85*(2), 413–431. https://doi.org/10.1111/j.1365-246x.1986.tb04521.x

Yao, H., & Van Der Hilst, R. D. (2009). Analysis of ambient noise energy distribution and phase velocity bias in ambient noise tomography with application to SE Tibet. *Geophysical Journal International*, *179*(2), 1113–1132. https://doi.org/10.1111/j.1365-246x.2009.04329.x

Zhan, Z. (2020). Distributed acoustic sensing turns fiber-optic cables into sensitive seismic antennas. *Seismological Research Letters*, *91*(1), 1–15. https://doi.org/10.1785/0220190112

Zhan, Z., Tsai, V. C., & Clayton, R. W. (2013). Spurious velocity changes caused by temporal variations in ambient noise frequency content. *Geophysical Journal International*, *194*(3), 1574–1581. https://doi.org/10.1093/gji/ggt170

Ziegenbein, J. (1970). Spatial observations of short internal waves in the Strait of Gibraltar. *Deep-Sea Research*, *17*(5), 867–875. https://doi.org/10.1016/0011-7471(70)90004-5